Origin of the stratiform temperature response to strong convective events: the interaction between convective and dry circulations

Toni Mitovski and Ian Folkins

Department of Physics and Atmospheric Science, Dalhousie University, Halifax, NS, Canada

Correspondence to T. Mitovski (mitovski@dal.ca)

Abstract

We use 13 years (1998 - 2010) of rainfall estimates from the Tropical Rainfall Measuring Mission (TRMM) 3B42 dataset to identify high rain events located close to radiosonde or surface weather stations. This is done in four regions: the Western Tropical Pacific, Tropical Brazil, Southeast China, and Southeast United States. We then construct composite anomaly patterns of a large number of dynamical variables about these high rain events. These variables include temperature, relative humidity, surface pressure, Convective Available Potential Energy (CAPE), geopotential height, mass divergence, static stability, relative vorticity, and potential vorticity. One motivation of this analysis is to identify regional differences in the effect of strong convective events on the background atmosphere. The second motivation is to determine the physical origin of the stratiform temperature response to deep convection, consisting of warming in the upper troposphere and cooling in the lower troposphere. We show that the dynamical adjustment to the stratiform heating profile is slower than the dynamical adjustment to the full depth convective heating profile. This difference in response times accounts for the local dominance of the stratiform temperature response, promotes the growth of mid-level maxima in stability and potential vorticity, and helps generate positive anomalies in lower tropospheric relative humidity during high rain events. We also show that the enhanced mid-level potential vorticity is transported to the surface after peak rainfall by the induced dry stratiform circulation.

1. Introduction

Strong convective events impose characteristic temperature anomaly patterns on the background atmosphere. These anomaly patterns have two surprising features. First, they are quite small. Convective events often sustain rainfall rates in excess of 50 mm/day for an 8-hour period. If evenly distributed between 850 hPa and 100 hPa, the condensational heating from this rainfall rate would produce a column heating rate of 14.7 K/day. The observed column heating rate during high rain events over the tropical oceans is less than 0.25 K/day, and is usually negative prior to peak rainfall. Second, while stratiform clouds generate roughly 40 % of tropical rainfall, convective clouds generate roughly 60 % [*Schumacher and Houze*, 2003]. The full depth convective heating profile might therefore be expected to dominate the local temperature response. Instead, the local temperature response is dominated by the stratiform heating profile, consisting of heating in the upper troposphere and cooling in the lower troposphere [*Sherwood and Wahrlich*, 1999; *Mapes et al*., 2006; *Mapes et al*., 2009; *Mitovski et al*., 2010; *Zuluaga and Houze*, 2013].

The weakness of the observed temperature response to convective events in the tropics can be attributed to an induced dynamical circulation. The dynamical adjustment to moist convective heating involves upward motion and adiabatic cooling in the background atmosphere, and generates a larger scale dry circulation in which the full depth convective heating and drying are transported to larger spatial scales. This characteristic of the tropical atmosphere has been exploited in a widely used dynamical theory known as the Weak Temperature Gradient approximation [*Sobel et al*., 2001], in which the induced dynamical cooling exactly cancels the local convective heating. This theory can not account for the observed local stratiform temperature response, however, because of the imposed exact cancellation between the convective and dynamical heating terms.

We use routine radiosonde observations to construct composite anomaly patterns of a large number of meteorological variables about high rain events. These variables include temperature, relative humidity, column water vapor, Convective Available Potential Energy (CAPE), geopotential height, mass divergence, relative vorticity, stability, and potential vorticity. The TRMM 3B42 dataset is used to identify 2x2 grid cells in which the rain rate exceeds a particular threshold. The observed anomaly patterns are then used to construct a conceptual model of the interaction between convective and dry circulations during the evolution of high rain events. The conceptual model would be most appropriate on the space and time scales of the rain events we select, which is several hundred km and 1-2 days. We argue that the dynamical response to stratiform heating is slower than the dynamical response to full depth convective heating, and that this difference in time lags accounts for the dominance of the local stratiform temperature response.

The TRMM 3B42 gridded rainfall product is available from 1998 to the present. We look for radiosonde or surface measurements that are co-located, and within 48 hours, of the TRMM high rain events. To obtain better statistics, this procedure is repeated at many radiosonde stations, using a large number of rain events from 1998 to 2010. This approach has been followed using routine radiosonde profiles [*Sherwood and Wahrlich*, 1999; *Mitovski et al*., 2010], measurements from field campaigns [*Sobel et al*., 2004; *Mapes et al*., 2006; *DeMott et al*., 2007; *Mapes et al*., 2009], satellite data [*Masunaga*, 2012], and re-analysis data [*Benedict and Randall*, 2007; *Rapp et al*., 2011]. Some of the anomaly patterns shown in this paper, especially with respect to temperature and relative humidity, therefore reproduce known relationships. However, this procedure has not been used to calculate the anomaly patterns of other meteorological variables such as geopotential height and potential vorticity. Where possible, the anomaly patterns are calculated using groups of radiosonde stations in four regions: the Western Tropical Pacific, Tropical Brazil, the Southeast United States, and Southeast China. This approach enables us to identify similarities and differences in the interaction between deep convection and the background atmosphere between the four regions.

2. Datasets

2.1 Rainfall Data

The TRMM 3B42 gridded rainfall dataset is constructed from several satellite borne sensors. These include a precipitation radar, multichannel microwave radiometer, and visible and infrared sensors [Kummerow et al. 1998, Liu et al. 2012]. The data is available at 3-h temporal (centered at 00:00, 03:00, 06:00, 09:00, 12:00, 15:00, 18:00, and 21:00 UTC), and 0.25 x 0.25 degree horizontal resolution. We used TRMM 3B42 rainfall to identify high rain events between Jan 1998 and Dec 2010.

2.2 Radiosonde Data

The Integrated Global Radiosonde Archive (IGRA) dataset is stored at the National Climatic Data Center (NCDC) [*Durre at al*., 2006]. We used data from 53 radiosonde locations from the 1998 – 2010 time period. The locations of these stations are shown as open squares in Figure 1**,** and are located in four regions: 6 from the Western Tropical Pacific, 11 from Tropical Brazil, 19 from the Southeast United States, and 17 from Southeast China. The soundings provide temperature and relative humidity profiles at variable vertical resolution. Within the Southeast United States region, there were on average 42 temperature and relative humidity measurements below 100 hPa. The comparable numbers for the radiosonde stations in the Western Tropical Pacific, Tropical Brazil, and Southeast China regions, are 39, 26, and 14, respectively. The soundings also provide horizontal wind measurements at the surface and at the standard pressure levels of 1000, 925, 850, 700, 500, 400, 300, 250, 200, 150, and 100 hPa. Although some of the IGRA soundings are available every 6 hours, the majority of the soundings are available twice per day at the 00:00 and 12:00 UTC standard synoptic times.

The divergence and vorticity anomaly calculations require simultaneous horizontal wind measurements from triangular radiosonde arrays. For these variables, we used 2 arrays from the Western Tropical Pacific, 5 arrays from Tropical Brazil, 14 arrays from the Southeast United States, and 17 arrays from Southeast China. The average area of the Western Tropical Pacific arrays was 296,000 km^2 (roughly equal to the area of a 5x5-degree grid box at the equator), 57,000 km^2 for the Southeast United States arrays (roughly equal to a 2.5x2.5-degree grid box at 30 N), 207,000 km^2 for the Tropical Brazil arrays, and 31,000 km^2 for the Southeast China arrays.

2.3 Hourly Surface Data

Over land, convective precipitation usually peaks in the late afternoon [*Nesbitt and Zipser*, 2003]. The rain events used to construct the anomaly patterns over land also occur more frequently in the late afternoon. Within a given region, the radiosonde profiles will usually occur at two fixed local solar times. The incomplete diurnal sampling of the radiosondes, in combination with the existence of diurnal cycles in both the rain event frequency and the meteorological variables, will introduce biases into the calculation of our anomaly patterns. It is therefore important that, where possible, the radiosonde anomaly patterns be validated against surface measurements with better temporal resolution.

The Integrated Surface Hourly (ISH) dataset consists of surface weather observations from about 20,000 worldwide-distributed stations [*Lott et al*., 2001]. The data is archived at the NCDC, and contains hourly and synoptic (3-hourly) surface weather observations of several variables, including temperature, relative humidity, and pressure. We used ISH data between 1998 and 2010, from surface stations, which were co-located with the 53 IGRA radiosonde stations shown in Figure 1.

2.4 Global Positioning System Data

We also used Global Positioning System (GPS) radio occultation temperature measurements from the Constellation Observing System for Meteorology, Ionosphere and Climate (COSMIC) six-satellite constellation [*Anthes et al*., 2008], downloaded from the COSMIC Data Analysis and Archive Center (CDAAC). There are approximately 2,000 high-vertical resolution (~100 m in the troposphere) COSMIC temperature profiles over the earth per day. Over a particular region, the

COSMIC profiles are distributed roughly uniformly in local solar time. They can therefore also be used to help determine whether the calculated radiosonde temperature anomaly patterns over land exhibit a diurnal bias. We used COSMIC temperature profiles within the Southeast United States (between 30 N and 40 N and between 85 W and 100 W) and Southeast China (between 25 N and 35 N and between 103 E and 118 E) regions shown in Figures 1c and 1d. For both regions, we restricted attention to the convective summer season (June July and August) from 2006 to 2010.

3. Rain Event Definition

In the construction of the radiosonde and surface station anomaly patterns, high rain events were considered to occur at locations where the mean TRMM 3B42 rainfall over a 2 by 2 degree area centered at each station exceeded 1.5 mm/h over a TRMM 3 hour time interval. For the calculation of the mass divergence and relative vorticity anomaly patterns, we used triangular radiosonde arrays, and rain events were defined using the average TRMM 3B42 rain rate within each array. For the Southeast United States and Southeast China regions, we restricted attention to June, July, and August. For the tropical Brazil and the Western Tropical Pacific regions, we used rain events from the entire year.

Figure 2a shows composite TRMM 3B42 2x2-degree rain event profiles from each of the four regions. The rain event profiles were constructed from events co-located with radiosonde or surface stations, rather than from rain events within the variably sized radiosonde arrays. The rain event profiles are quite similar, partly reflecting the use of a common rain event threshold. High rain events develop slightly more rapidly over the three land regions than the Tropical Western Pacific. Rainfall starts to increase roughly 9 hours prior to peak rainfall, and drops to near background levels roughly 9 hours after peak rainfall.

GPS COSMIC temperature profiles were also used to construct temperature anomaly patterns about high rain events. Within a particular region, the GPS profiles tend to be randomly distributed. In order to identify high rain events co-located with GPS temperature profiles, we first calculated the mean TRMM 3B42 rain rate in 2x2 grid boxes, separated from each other by 1 degree. For example, the Southeast United States region shown in Figure 1c enclosed an area between 30-40 N and 85-100 W. Within this region, we calculated the mean rain rate in 10 x 15 = 150 overlapping 2x2 grid boxes, and searched for GPS temperature profiles within each box. The Southeast China region shown in Figure 1d enclosed an area between 25-35 N and 103-118 E, and was also partitioned into 150 overlapping boxes.

Figure 2b shows the variation in average rain rate as a function of radial distance from the high rain events. The rain events of the various regions have a similar spatial scale, with the rain rate typically decaying to a near background value within about 400 km of peak rainfall.

4. Diurnal Variability

Figure 3a shows the average diurnal variation of the TRMM 3B42 rain rate within each of the four regions. Within the three land regions the rainfall rate peaks in the late afternoon or early evening. The Tropical Western Pacific rainfall rate exhibits a small peak in the early morning. Figure 3b shows the diurnal variation in the frequency of occurrence of the rain events used to construct the radiosonde temperature anomaly patterns. The diurnal variation in the rain event frequency is similar to the diurnal variation in the rain rate itself.

Figure 4 shows the number of IGRA radiosonde profiles within each region that occurred within 48 hours of a rain event, and could be used in the construction of the temperature anomaly patterns. Within the Southeast United States, there were approximately 21,000 profiles at 06 and 18 h local solar time available from the 1998 – 2010 time period. We used 25,000 profiles from Tropical Brazil (08 and 20 h local solar time), 55,000 profiles from Southeast China (also at 08 and 20 h local solar time), and roughly 80,000 soundings from the Tropical Western Pacific, distributed at local solar times of 00, 09, 10, 11, 12, 21, 22, and 23 h. The broader range of local solar times from the Tropical Western Pacific reflects the broader longitudinal distribution of the radiosonde stations in this region.

5. Results

5.1 Temperature anomaly patterns from Radiosondes

Once a rain event at a radiosonde station had been identified, we searched for radiosonde launches that had occurred within 48 hours of the rain event. These soundings were then assigned to 3-h bins, based on the difference between the radiosonde launch and rain event times. At each location, radiosonde measurements were used to define climatological temperature profiles for each launch time, month, and year, and were used to convert the temperature profiles to temperature anomaly profiles. We then averaged the temperature anomaly profiles within each 3-h time bin.

The composite temperature anomaly patterns generated using the above procedure within each region are shown in Figure 5a, 5b, 5c, and 5e. For all regions, high rain events give rise to an upper-level warming centered at 300 hPa that is coincident with peak rainfall. With the exception of Southeast China, the regions also show a 700 hPa lower tropospheric cooling coincident with peak rainfall. Each region shows a strong boundary layer cooling (below 900 hPa) after peak rainfall.

This cooling is significantly larger and more persistent over the three land regions than over the Tropical Western Pacific. Deep convection over the three land regions is preceded by a warm anomaly in the lower troposphere. Over Tropical Brazil and Southeast China, this warming extends upward from the surface to 800 hPa, but extends to 600 hPa over the Southeast United States.

The details of the temperature anomaly patterns shown in Figure 5 will be sensitive, to some degree, to the assumptions used to define the rain events. For example, the use of a larger rain event threshold would be expected to generate larger temperature anomalies. It has been shown, however, that the shapes of the temperature anomaly patterns are not sensitive to the value of the rain event threshold or the assumed event area [*Mitovski et al*., 2010].

5.2 Temperature anomaly patterns from GPS

The GPS COSMIC temperature profiles were used to also construct temperature anomaly patterns of the Southeast United States and Southeast China regions. During the summer convective season (JJA) between 2006 and 2010, there were 2,111 profiles from the United States, and 1,538 profiles from China, which were co-located within 48 hours of a TRMM rain event. The COSMIC temperature anomaly patterns from these two regions are shown in Figure 5d and 5f. Although the COSMIC and radiosonde temperature anomaly patterns are in good overall agreement, the COSMIC boundary layer cooling is much smaller than the boundary layer cooling obtained from the radiosonde data. There are several reasons why the COSMIC temperature anomaly patterns may be less accurate near the surface. COSMIC provides vertical profiles of atmospheric refractivity, which can be used to calculate the vertical profile of atmospheric density [*Anthes et al*., 2008]. Variations in water vapor can be expected to more strongly affect the atmospheric density at higher temperatures closer to the surface. In the absence of an independent method of constraining the water vapor profile, the relative accuracy of the COSMIC temperature retrievals can be expected to be smaller at lower altitudes. The refractivity gradient at the top of the boundary layer frequently exceeds the critical refraction, which can result in a systematic negative refractivity bias in the radio occultations within the boundary layer [*Xie et al*., 2012]. Finally, the number of COSMIC temperature retrievals decreases toward the surface, especially for altitudes below 2 km [*Anthes et al*., 2008].

5.3 Anomalies in Pressure, Temperature, and Relative Humidity at the Surface

Figure 6 shows the response of surface temperature, surface relative humidity, and surface pressure to high rain events in each of the four regions, calculated from both the radiosonde and surface weather station data. In general, the radiosonde anomaly profiles (solid lines) are in good agreement with the profiles generated by higher temporal resolution surface measurements (dotted lines).

The top row of Figure 6 shows the response of surface temperature to high rain events. The two mid-latitude regions show larger surface cooling than the two tropical regions. This is consistent with Figure 5, which also shows greater persistence and depth in the boundary layer cooling over land. One explanation for this difference is that convection over land tends to develop under conditions of lower relative humidity than convection over the tropical oceans. Downdrafts over land would therefore be expected to exhibit stronger negative buoyancies, have a higher probability of penetrating the boundary layer, and possibly, generate more persistent cooling.

The middle row of Figure 6 shows the response of surface relative humidity to high rain events. Within all four regions, convective rainfall generates a sharp increase in surface relative humidity that is coincident, or slightly lags, peak rainfall. The size of the relative humidity increase scales with the size of the temperature decrease. The relative humidity increase of the two mid-latitude regions is larger than the increase of the two tropical regions.

The bottom row of Figure 6 shows the surface pressure response to high rain events. The surface pressure anomalies show stronger regional differences than the temperature and relative humidity anomalies. In the Tropical Pacific, there is a 0.5 hPa minimum in surface pressure 10 hours prior to peak rainfall, followed by a small local maximum that slightly lags peak rainfall. Over Tropical Brazil, there is a more rapid increase in surface pressure during high rain events. In the two mid-latitude regions, high rain events are associated with larger 1-2 hPa reductions in surface pressure over a 2-3 day timescale.

Although the radiosonde and surface station anomaly patterns are in good overall agreement, the radiosonde surface pressure anomalies within the Southeast Unites States, and to a lesser extent within Southeast China and Tropical Brazil, are significantly different from the surface station pressure anomalies. These deviations have a 12-hour periodicity. The black curve of the top panel of Figure 7 shows the average diurnal cycle in surface pressure from the Southeast United States surface stations. The red curve shows the diurnal cycle in surface pressure using measurements when the rain rate of the local grid cell exceeded 1 mm/h. The difference between the two curves shows that rainfall during the evening and early morning is associated with lower surface pressure. The bottom panel of Figure 7 shows that the surface pressure response to high rain events depends on the time at which the rain event occurs. Each response curve is constructed from high rain events having a common TRMM time, converted here to the approximate local solar time. Rain events which occur at 21, 00, and 03 local solar time give rise to much larger decreases in surface pressure, relative to the mean surface pressure at that local time, than do rain events in the late afternoon.

The existence of a diurnal cycle in the surface pressure response to high rain events leads to errors when the twice daily radiosonde profiles are used to construct the surface pressure anomaly patterns. The twice daily radiosonde launches occur at local solar times of 6 and 18 h. The middle panel of Figure 7 shows the surface pressure response constructed from the individual sondes, as well as the combined response shown previously in Figure 6. For the two individual response curves, there is a 24 h oscillation generated by changes in the local solar time of the rain events. For example, the curve generated using the 6 LT radiosonde launches and the curve generated using the 18 LT radiosonde launches both show maxima associated with rain events occurring at 15 LT, and minima associated with rain events occurring at 00 LT. The pattern of this response is consistent with Figure 7c, which shows a weaker surface pressure response to rain events occurring in the late afternoon, and a stronger response to rain events at night. The overall surface pressure response in Figure 7b, indicated by the dashed line, is equal to the average of the two individual radiosonde curves, weighted by the relative frequency of the rain events used to construct the two curves. Inspection of the middle panel shows that the 12 hour oscillation in the combined radiosonde response is an artifact generated from the 24 hour oscillations of the two individual curves.

5.4 Radial Distribution of the Convective Temperature Response

The temperature anomaly patterns shown in Figure 5 show the time evolution of the local temperature response to deep convection, but give no indication of the spatial scale over which these temperature anomalies extend. In this section, the radiosonde measurements are used to calculate the temperature response to the TRMM high rain events as a function of the radial distance from the events. We first identified all 2x2 rain events within a particular region, and then searched for radiosonde measurements within 1000 km of the rain event which had occurred within 3 h of the rain event time. The radiosonde temperature profiles were then stored in 50 km bins, based on the distance between the rain event and the radiosonde location. Each temperature profile was converted to an instantaneous anomaly profile by subtracting the climatological launch-time/monthly/yearly temperature profile at that location. The temperature anomaly profiles within each 50-km bin at each pressure level were then averaged, and the results shown in Figure 8**.**

The dominant feature of the radial temperature response is an upper level (300 hPa) warming that extends roughly 800 km outward from the rain event. All four regions also exhibit a strong near surface (below 900 hPa) cooling that extends roughly 300 km outward from the rain event. The Tropical Pacific Ocean and Southeast United States regions exhibit a strong lower tropospheric cooling between 800 hPa and 500 hPa. This lower tropospheric cooling is less pronounced over Tropical Brazil, and absent over Southeast China. Figure 8 shows that the regional differences in the local convective temperature response shown in Figure 5 are not restricted to the immediate environment of deep convective events, but extend to much larger spatial scales.

5.5 Relative Humidity

The IGRA radiosonde dataset supplies vertical profiles of water vapor pressure, which can be converted to relative humidity. At temperatures below 0 C, we normalized the vapor pressure by the saturation vapor pressure over ice [*Emanuel*, 1994]. In general, radiosonde measurements of vapor pressure are less accurate at colder temperatures [*Kley et al*., 2000]. The relative humidity was therefore not calculated for pressure levels above 200 hPa. Figure 9 shows the relative humidity response to high rain events, calculated using a procedure similar to that used for the temperature anomaly patterns. Within each region, peak rainfall is associated with values of relative humidity that exceed 80% at most altitudes. The gradual moistening of the lower troposphere prior to high rain events has been attributed to the influence of congestus clouds [*Takayabu et al*., 1996; *Mapes et al*., 2006], but this interpretation has been recently challenged [*Hohenegger and Stevens*, 2013]. Rain events within the Southeast United States occur within a background atmosphere that is significantly drier than the other three regions, particularly in the upper troposphere.

The radial relative humidity response to high rain events was calculated using the same procedure used to calculate the radial temperature response. Figure 10 shows that high rain events generate strong positive anomalies in upper tropospheric humidity that extend roughly 400 km outward from the high rain events. The relative humidity patterns of the Southeast United States and Tropical Western Pacific regions are very similar, except that the enhancement in the Pacific region extends to longer distances. The upper tropospheric relative humidity enhancement of the Tropical Brazil region is much smaller than the other regions.

5.6 Total Column Water Vapor

The relative humidity and temperature measurements of the radiosonde profiles can be used to calculate the total column water vapor, defined here as the mass of water vapor per unit area between the surface and 200 hPa (also known as the precipitable water). The upper panel of Figure 11 shows the column water vapor response to high rain events within each region, while the lower panel of Figure 11 shows the column water anomaly. Rain events in the Southeast United States occur at much lower values of column water than the other three regions. However, the change in column water during high rain events in the Southeast United States is very similar to the change in Southeast China and the Tropical Pacific (7 -10 kg/m2). Rain events in Tropical Brazil are associated with smaller increases in column water (less than 4 kg/m2).

5.7 Convective Available Potential Energy

The existence of air parcels near the surface with positive Convective Available Potential Energy (CAPE) is a precondition for moist convection. There are a variety of methods for calculating CAPE. We start with air parcels near the surface whose pressure, temperature, and relative humidity are equal to the values given by a radiosonde profile at a particular pressure level. We then lift the air parcel, subject to the assumptions of constant moist static energy and total water (i.e. no condensate removal), no mixing, and no ice formation. The CAPE of the profile from a particular starting level is then calculated using the following expression.

$$\mathrm{CAPE} = \int_{Z_{LFC}}^{Z_{LNB}} g\left(\frac{T_{dp} - T_{ve}}{T_{ve}}\right)dz, \quad (1)$$

T_{dp} refers to the density temperature of the air parcel. The density temperature is an effective temperature for calculating density in which the condensate mass is included. T_{ve} is the virtual temperature of the environment, Z_{LFC} is the level of free convection, and Z_{LNB} is the level of neutral buoyancy for that parcel.

The radiosonde profiles of the Western Tropical Pacific and Southeast United States regions had sufficient vertical resolution to resolve the vertical structure of boundary layer CAPE. Figure 12 shows the variation in CAPE, and the CAPE anomaly, about high rain events from the two regions. Deep convection is associated with strong negative anomalies in CAPE, which maximize at roughly 800 J/kg near the surface several hours after peak rainfall. This CAPE reduction is presumably associated with some combination of preferential entrainment of higher moist static energy air parcels from the boundary layer by convective updrafts, and by the injection of lower moist static energy air into the boundary layer from the mid-troposphere [*Zipser*, 1977]. Over the tropical oceans, the CAPE reduction extends over a vertical depth of roughly one km and persists for about 20 hours.

Figure 12 also shows that, while the CAPE anomalies preceding rain events from the Western Tropical Pacific region were weak, the CAPE anomalies preceding rain events within the Southeast United States were strongly positive. Due to the diurnal cycle in CAPE over land [*Dai et al*., 1999] and the higher frequency of rain events during the late afternoon, some of the CAPE enhancement shown in Figure 12b preceding peak rainfall can be attributed to the diurnal cycle. The diurnal cycle also contributes to a 24 hour oscillation in CAPE prior to peak rainfall. Figure 12d shows the CAPE anomaly, in which the diurnal effect has been reduced by subtracting from each CAPE measurement the mean value of CAPE for each particular radiosonde launch time, station, and month. The largest CAPE anomaly of roughly 600 J/kg occurs at 950 hPa, 6 hours prior to peak rainfall. After peak rainfall, there is a negative CAPE anomaly of roughly 400 J/kg that is largest near the surface.

Within the Southeast United States CAPE and CAPE anomaly patterns shown in Figure 12, there is a 12 hour oscillation that mainly occurs prior to peak rainfall. This oscillation is an artifact generated by the same mechanism which produces the surface pressure oscillation shown in Figure 7. The top panel of Figure 6 shows that the surface temperature errors in the Southeast United States introduced by this sampling bias are small. However, these errors have a larger relative impact on CAPE.

5.8 Geopotential Height

Geopotential height profiles were calculated from the surface pressure, temperature, and relative humidity measurements of the individual radiosonde profiles. The geopotential height at the surface of each location was set equal to the local surface station altitude. We used stations whose altitude was less than 200 m. We then iteratively calculate the geopotential height upward from the surface using the hypsometric equation. This equation defines the geopotential height at a pressure level n in terms of the geopotential height at a lower pressure level n-1, the virtual temperature at levels n-1 and n, and the pressure thickness dp.

$$\mathrm{GPHT}_n = \mathrm{GPHT}_{n-1} + R_d\left(\frac{T_{v,n-1} + T_{v,n}}{2g}\right)\mathrm{d}\ln p. \qquad (2)$$

In this equation, p refers to pressure in Pascals, R_d to the specific gas constant of dry air (287.04 $\mathrm{Jkg^{-1}K^{-1}}$), Tv to the virtual temperature of an air parcel, and g to standard gravity (9.806 $\mathrm{ms^{-2}}$), and dlnp is defined as

$$\mathrm{d}\ln p = \frac{p_{n-1} - p_n}{0.5(p_{n-1} + p_n)} \; . \qquad (3)$$

To obtain the geopotential height anomaly, we subtracted from each geopotential height the mean geopotential height for that station, month, and radiosonde launch time. We then grouped the resulting geopotential height anomaly profiles of each region in 3-hour time bins about their respective rain events. Figure 13 shows the geopotential height anomaly patterns associated with the high rain events of each region. The anomaly pattern of the Southeast Unites States exhibits a 12 hour oscillation. This oscillation is stronger in the lower troposphere, and can be attributed to the 12 hour oscillation in lower tropospheric surface pressure discussed earlier.

The geopotential height anomaly patterns of the four regions show some common features. Each region shows a strong positive geopotential height anomaly in the upper troposphere centered at 200 hPa. This anomaly is generated mainly by the upper tropospheric 300 hPa warm anomaly shown in Figure 5. Within each region, the geopotential anomalies change sign from positive to negative near 400 hPa.

In the two tropical regions, the negative mid-level geopotential anomaly is largest at 500 hPa, and roughly symmetric about peak rainfall. The onset of the reductions in lower tropospheric geopotential height begin prior to the lower tropospheric cooling shown in Figure 5a, and can be mainly attributed to reductions in surface pressure. For example, the lower left panel of Figure 6 shows that the surface pressure of the Western Tropical Pacific region decreases by roughly 0.6 hPa prior to peak rainfall. This would generate a geopotential height decrease of roughly 5.2 m, which is comparable with the negative anomalies in lower tropospheric geopotential height prior to peak rainfall shown in Figure 13a.

In the two mid-latitude regions, negative surface pressure anomalies several days prior to peak rainfall generate negative geopotential height anomalies in the boundary layer. As peak rain rates develop, the cold anomalies in the boundary layer and mid-levels contribute to the intensification and upward extension of these negative geopotential height anomalies to 400 hPa. These negative mid-level anomalies are much stronger, deeper, and more persistent than those observed in the tropics.

5.9 Mass Divergence

At a given pressure level, the net horizontal mass inflow or outflow from a convecting region can be estimated using horizontal wind measurements from radiosonde arrays. We calculated the mass divergence of the triangular arrays shown in Figure 1 using the following expression.

$$\nabla \cdot \vec{V} = \sum \frac{\vec{V} \cdot \vec{n} dl}{A}, \qquad (4)$$

$\vec{V} \cdot \vec{n}$ refers to the wind component normal with respect to a line that connects two points of the array, dl is the distance between the two points, and A refers to the surface area of the array.

The number of divergence profiles available to construct the anomaly patterns is usually much less than the number of temperature or relative humidity profiles, partly because a divergence calculation require a complete ring of simultaneous horizontal wind measurements. The native resolution TRMM 3B42 dataset was used to calculate the average rainfall rate within the arrays shown in Figure 1. The rain event frequency is in general smaller for larger arrays. On average, there were 164 divergence profiles available per 3 h time bin from the two arrays in the Western Tropical Pacific, 205 profiles from the 14 arrays in the Southeast United States, 414 profiles from the 17 arrays in the Southeast China, and 102 profiles from the 5 arrays in the Equatorial Brazil.

Figure 14 shows the divergence anomaly patterns of each region. The four patterns are quite similar. The dominant feature of each pattern is a strong divergence maximum in the upper troposphere (200 hPa). This divergence maximum occurs near peak rainfall, but in three of the regions shows a tendency for stronger persistence after peak rainfall. Each region also shows a strong convergence feature in the boundary layer prior to peak rainfall, extending from the surface to 800 hPa. In the Western Tropical Pacific, this feature occurs 6 hours prior to peak rainfall. For rain events within the three land regions, the time difference between the boundary layer divergence maximum and peak rainfall is roughly equal to 3 hours.

The divergence anomaly pattern of the Western Tropical Pacific region shown in Figure 14 exhibits an antisymmetric mid-level divergence dipole about peak rainfall [*Thompson et al.*, 1979; *Mapes et al.*, 2006; *Mitovski et al.*, 2010]. Within the three land regions, there is a tendency for mid-level divergence to occur prior to peak rainfall and mid-level convergence to occur after peak rainfall. However, these divergence features occur closer to peak rainfall than in the Western Tropical Pacific.

5.10 Stability

The radiosonde temperature profiles were used to calculate the static stability using the following expression.

$$\sigma = \left(-\frac{T}{\theta}\right)\left(\frac{\partial\theta}{\partial p}\right). \qquad (5)$$

Figure 15 shows the impact of high rain events on the atmospheric stability of each region. Rain events tend to destabilize the upper tropopause (200 hPa), stabilize the mid-troposphere (400 hPa), destabilize the lower troposphere (700 hPa), and stabilize the boundary layer (below 900 hPa). Cloud resolving model simulations show that convective clouds tend to preferentially detrain at heights where their buoyancy is decreasing [*Bretherton and Smolarkiewicz*, 1989]. The mid-level stability enhancement would therefore favor the detrainment of cumulus congestus clouds in the 500 – 400 hPa layer [*Zuidema*, 1998; *Johnson et al.*, 1999; *Bister and Mapes*, 2004; *Folkins*, 2009]. The mid-level stability enhancement is stronger over the two mid-latitude land regions. Figure 8 shows that the spatial scale of these stability enhancements is roughly 1000 km.

5.11 Relative Vorticity

Relative vorticity was calculated from the horizontal wind measurements of a radiosonde array using the following expression.

$$\zeta = \sum \frac{V_p dl}{A}, \qquad (6)$$

V_p refers to the wind component parallel to a line connecting two points in the array, dl to the distance between the two points, and A to the surface area of the array.

Unfortunately, the vorticity anomaly patterns of the two tropical regions were irregular and did not show strong features. This can probably be attributed to the weakness of the Coriolis parameter at the latitudes characteristic of the radiosonde arrays of these two regions, which would weaken the relative impact of the divergence term on the local vorticity budget. Figure 16 shows the vorticity anomaly patterns of the two mid-latitude regions. Within the Southeast China and Southeast United States regions, positive relative vorticity anomalies develop in the boundary layer 1 day prior to peak rainfall. These features are presumably associated with the coincident development of boundary layer convergence. At peak rainfall, the positive vorticity anomalies intensify and grow vertically to 400 hPa. The timing in the growth and vertical extent of these vorticity anomalies is consistent with the mid-level convergence features shown in Figure 14. Both regions also show a strong negative (anticyclonic) vorticity anomaly in the upper troposphere, as would be expected to develop in response to the strong upper tropospheric outflow features shown in Figure 14.

5.12 Potential Vorticity

Potential vorticity (PV) was calculated from the temperature and horizontal wind profiles of the radiosonde arrays using then following expression.

$$PV = (\zeta + f)\left(-g\frac{\partial\theta}{\partial p}\right), \qquad (7)$$

The PV and PV anomaly patterns about high rain events within the Southeast United States and China regions are shown in Figure 17. The tropopause is indicated by the strong vertical PV gradient near 200 hPa. In both regions, high rain events generate strong negative PV anomalies along the tropopause. The development of this anomaly is consistent with the upward transport of low PV air from the boundary layer within convective updrafts, and with the reduction in convective heating (decreased stability) in going from the troposphere to the stratosphere.

Figure 17 also shows that high rain events of the two regions are associated with positive PV anomalies that extend from the surface to 400 hPa. The stratiform type temperature response shown in Figures 5 and 8 would be expected to generate positive stability and PV anomalies in the mid-troposphere. It has been previously shown that squall lines with trailing stratiform clouds generate positive PV anomalies in the mid-troposphere [*Hertenstein and Schubert*, 1991]. Figure 17 also shows that high rain events in the Southeast United States are associated with strong positive PV anomalies near the surface. These increase are consistent with the increase in boundary layer stability that occurs during high rain rates.

6. Temperature and Relative Humidity Tendencies

Figure 18a shows the temperature tendency pattern about high rain events calculated from the Western Tropical Pacific temperature anomaly pattern shown in Figure 5a. The pattern is clearly dominated by the development of a stratiform temperature response prior to peak rainfall, and the erosion of this response after peak rainfall. Figure 19a shows the column heating rate of the free troposphere during the evolution of high rain events in each region. It was calculated from the observed temperature tendency pattern, with the tendency of each layer between 850 hPa and 100 hPa weighted by its pressure fraction. Within each region, the column mean heating rate is less than 1 K/day. The column temperature tendency is smallest in the Western Tropical Pacific region, were it is less than 0.5 K/day. If the condensational heating from the peak rain rate within this region of 66 mm/day were evenly distributed between 850 hPa and 100 hPa, it would generate a column mean heating rate of 19.4 K/day. The local column heating rate of this region is therefore roughly two orders of magnitude smaller than the condensational heating associated with the local rain rate.

Figure 18d shows the evolution of the domain averaged vertical motion during high rain events within the Western Tropical Pacific radiosonde arrays. The pressure velocity was calculated from the divergence anomaly pattern shown in Figure 14a, the climatological divergence profile of each array, and by imposing the boundary condition $\omega = 0$ at the 100 hPa pressure level. Prior to peak rainfall, there is strong upward motion throughout the troposphere, with somewhat larger ascent in the lower troposphere. After peak rainfall, the vertical motion is mainly confined to the upper troposphere [*Mapes et al*., 2006].

Figure 18b shows the temperature tendency pattern associated with the vertical motion pattern shown in Figure 18d. It was calculated by multiplying the calculated vertical pressure velocity by the appropriate static stability. The upward motion generates cooling rates that at times exceed 10 K/day. The extremely small column heating rates shown in Figure 19a can therefore be mainly attributed to a near cancellation between the heating rates generated by the convective circulations and the mean vertical motion within the radiosonde arrays.

7. Convective and Dry Circulations

We adopt a conceptual model in which the total dynamical response to convection can be decomposed into convective and dry circulations. Figure 20c shows a convective circulation generated by a precipitating convective cloud with no downdrafts. The buoyancy driven upward motion within the cloud generates subsidence in the cloud environment. On short timescales, these circulations should be contained within regions whose size is comparable with the areas of the radiosonde arrays used here. Overturning convective scale circulations within these regions will therefore generate temperature and geopotential height anomalies within the array, but will not directly generate non-zero mass inflows or outflows along the boundaries of the arrays. Figure 20d shows the dry circulation generated by the geopotential height anomalies of the convective scale circulation. At upper levels, positive anomalies in geopotential height generate mean outward pressure gradient accelerations that will drive, with some time lag, a divergent outflow. By mass conservation, this divergent outflow must be balanced by mean upward flow within the domain. The adiabatic cooling associated with this mean upward motion will diminish the geopotential height anomalies produced by the original convective scale circulation. The convective and dry circulations defined here appear to be analogous to Stages 1 and 2 of a previous discussion of convective adjustment [*Raymond et al.*, 2009].

Figure 20a shows the convective circulations associated with the three most important categories of precipitating convective clouds: congestus clouds (outflow in the mid-troposphere), deep clouds (outflow in the upper troposphere), and stratiform anvils (cloud base near the melting level with evaporatively driven downdrafts below). Figure 20b shows the three dry circulations that would be produced by the geopotential height anomalies of the three convective circulations. In order to generate domain averaged vertical motions able to damp the temperature anomaly patterns generated by the three convective circulations, the three dry circulations must produce net horizontal inflows and outflows at various altitudes along the boundaries of the domain.

Within a region undergoing precipitating convection, there will in general be some combination of the three basic convective circulations, their associated dry circulations, and other externally forced large scale dynamical motions. However, the divergence anomaly patterns indicate that the convective and dry circulations preferentially occur at particular stages of the evolution of high rain events. The divergence anomaly pattern of the Western Tropical Pacific region is shown in Figure 14a. Prior to peak rainfall, there is a divergence at mid-levels coupled with convergence in the boundary layer. This pattern is consistent with the presence of lower tropospheric ascent within the radiosonde array, a circulation labeled as dry congestus in Figure 20b. This circulation would contribute, prior to peak rainfall, to the observed negative tendency in lower tropospheric temperature and a positive tendency in lower tropospheric relative humidity.

The three circulations of Figure 20 able to contribute to the development of the low level cooling at peak rainfall are the dry congestus circulation, the dry deep circulation, and the convective stratiform circulation. The simultaneous development of the upper level warm anomaly suggests that the convective stratiform circulation plays the largest role in the development of the peak rainfall temperature anomaly pattern. The dominance of the local stratiform temperature response is somewhat surprising, given that only 40 % of tropical rainfall originates from stratiform clouds [*Schumacher and Houze*, 2003].

Figure 19b shows the time evolution of the upper tropospheric 200 hPa divergence during high rain events. The peak in upper tropospheric divergence lags peak rainfall by roughly 3 hours. The dry deep circulation is therefore nearly in phase with the rainfall rate, and rapidly exports the full depth convective warming and drying response of the convective deep circulation outside the radiosonde domain. This helps generate the near zero column heating rates within the domain shown in Figure 19a. Figure 19b also shows the time evolution of the mid-tropospheric 400 hPa divergence during high rain rates. The mid-level convergence feature lags peak rainfall by roughly 9 hours. This convergence feature is generated by the dry stratiform circulation (convergence at mid-levels and divergence at upper levels and in the boundary layer). The vertical motions associated with this circulation are shown in Figure 20. They generate temperature tendencies that contribute to the low level warming and upper level cooling that are required after peak rainfall to damp the stratiform temperature response. The low level descent from this circulation would also contribute to the strong negative tendency in lower tropospheric relative humidity after peak rainfall shown in Figure 18c. Because of the longer response time of the dry stratiform circulation, the temperature response of the initial convective stratiform circulation is permitted to accumulate within the radiosonde domain during the development phase of high rain events.

Figure 18b shows that the lower tropospheric temperature tendency from vertical advection after peak rainfall is small. This tendency would include contributions from the vertical motions of all three dry circulations. Presumably, a positive temperature tendency from the dry stratiform circulation is being offset by negative contributions from the dry deep and congestus circulations. Positive heating rates in the lower troposphere from the convective congestus or deep circulations would therefore also appear to be required to generate the observed net positive lower tropospheric heating rates after peak rainfall. The convective congestus circulation may therefore also play a role in damping the lower tropospheric cooling generated by the convective stratiform circulation.

The fast response of the dry deep circulation is likely to have an effect on the rate of development of strong convective events. The rapid export of the full depth warming signal from deep convection to larger spatial scales would prevent the reduction in convective instability that would otherwise be expected to occur due to increased local subsidence from deep convection, and by neutralizing deep subsidence drying, to the increase in column water during high rain events shown in Figure 11. Because, column water increases decrease the effect of entrainment on convective cloud buoyancy, the growth rates of convective events are likely to be partly controlled by the rate at which the dry deep circulation is able to export the full depth heating and drying to larger spatial scales.

Figure 17 shows that a mid-level PV maximum develops in response to high rain events in the Southeast United States and China, as would be expected from the heating profile of the convective stratiform circulation. The tongue of high PV extending downward from 400 hPa after peak rainfall, as shown in Figures 17a and 17b, is consistent with the development of the dry stratiform circulation. Due to the longer time lag of this circulation, mid-level positive stability and PV anomalies are permitted to accumulate within the radiosonde domains, which are subsequently advected by this circulation toward the surface.

The downward advection of the mid-level PV maximum after peak rainfall shown in Figure 17 may play a role in hurricane genesis. In the "top down" theory of hurricane genesis [Gjorgjievska and Raymond, 2013], a mid-level positive PV anomaly generated by the stratiform heating profile of a mesoscale convective system is advected toward the surface by evaporative cooling, where it then initiates the formation of a warm core anticyclone [Bister and Emanuel, 1997]. The timing of the downward transport shown in Figure 17 suggests that the downward advection of the mid-level PV anomaly can be initiated by the dry stratiform circulation. This downward transport would also, in general, reduce the moist static energy and relative humidity of the lower troposphere, unless the usual melting level minimum in moist static energy was sufficiently reduced by other processes.

Within climate models, buoyancy driven convective circulations are generated by the convective parameterization and are entirely contained within a model grid column, while the grid scale winds are generated mainly by horizontal pressure gradient and Coriolis accelerations. In climate models, there is therefore an absolute separation between the convective and dry circulations in terms of their spatial scale and physical origin, similar to what has been assumed here. However, an absolute separation between the two circulations is not likely to occur in nature [*Mapes*, 1997]. The initial stages of the dynamical adjustment to convective heating are mediated by the propagation of gravity waves outward from the sources of convective heating [*Bretherton and Smolarkiewicz*, 1989]. Our decomposition of this dynamical response into convective and dry circulations may be viewed as a simplification of this dynamical adjustment, but is physically motivated by the observed divergence and geopotential height anomaly patterns. This decomposition is useful to the extent that there exists a time lag between the convective and dry circulations. In the absence of a time lag, the individual vertical velocities of the two circulations would not be directly observable. The magnitude of the time lag between the convective and dry circulations is presumably related to the time required for a convective circulation to increase the geopotential height anomalies to the levels required to drive the larger scale dry circulation. If the convective circulation generates the required geopotential height anomalies very quickly, the time lag would be small, there would exist a near cancellation between the two vertical motions at all stages in the development of high rain events, and the temperature anomalies generated by the heating mode would be correspondingly reduced.

Convective heating generates gravity waves of various vertical wavelengths. The gravity waves generated by the deep convective heating mode preferentially generate waves having vertical wavelengths roughly twice the depth of the troposphere. The stratiform heating mode generates waves with a vertical wavelength roughly equal to the depth of the troposphere [*Mapes and Houze*, 1995]. Gravity waves with larger vertical wavelengths have faster propagation speeds. During a high rain event, the gravity waves generated by a convective heating profile within a radiosonde array will spread out from their convective sources, generate vertical motions within the domain, and horizontal winds along the boundaries. The time for this dynamical response to occur would be roughly equal to the size of the radiosonde array divided by the speed of the gravity wave. The gravity waves excited by the full depth convective heating mode have a speed of roughly 52 m/s, while those excited by the stratiform heating mode have a speed of 23 m/s [*Mapes and Houze*, 1995]. As mentioned earlier, the two arrays in the Western Tropical Pacific have an average area of 296,000 km^2, corresponding to a size of 545 km. The time lags associated with the full depth and stratiform heating modes should therefore be roughly 2.9 and 6.6 hours, respectively. This is roughly consistent with the observed time lags of 3 and 9 hours shown in Figure 19b.

8. Summary

We have used the TRMM 3B42 gridded rainfall dataset to identify 2x2 rain events in four regions: the Western Tropical Pacific, Tropical Brazil, Southeast China, and Southeast United States. Within each region, we selected rain events in close proximity to radiosonde or surface weather stations. These measurements were then used to construct composite anomaly patterns of a large number of meteorological variables about high rain events. One motivation of this analysis was to determine regional similarities and differences in the dynamical impact of strong convective events on the background atmosphere. The second motivation was to help determine the pathways by which the atmosphere attempts to return to a balanced state following moist convection, and to help understand how these pathways affect the evolution of convective systems.

Our analysis shows that there are many similarities in the effect of strong convective events on the background atmosphere between the four different regions. With the partial exception of

Southeast China, which appears to lack the 700 hPa cooling maximum, deep convection imposes a stratiform type temperature response on the background atmosphere. In all four regions, the upper tropospheric warming extends roughly 1000 km outward from deep convective events, indicating that deep convective events have a long range impact on the convective instability of their environment. The lower tropospheric cooling has a somewhat shorter horizontal extent, as would be expected from the slower propagation speed of the gravity waves excited by the stratiform heating mode. The upper tropospheric warming and lower tropospheric cooling generate increased stability at mid-levels. The mid-level stability increase can be expected to enhance convective detrainment in the mid-troposphere, and promote the development of the cumulus congestus mode. Strong cooling boundary layer develops after peak rainfall. The boundary layer cooling was somewhat deeper over the three land regions than the tropical ocean.

In two regions, we were able to calculate the time evolution of the vertical structure of CAPE in the boundary layer during high rain events. Within the Southeast United States region, the CAPE enhancement prior to peak rainfall was roughly 200 J/kg, while within the Western Tropical Pacific region, the CAPE enhancement was almost negligible (~ 40 J/kg). In both regions, the boundary layer cooling after peak rainfall contributes to the development of strong negative CAPE anomalies throughout the boundary layer.

There were some differences in the impact of strong convective events on the background atmosphere. The mid and lower tropospheric negative geopotential height anomalies that developed during and after high rain events in the two mid-latitude regions were much stronger, more vertically coherent, and more persistent, than in the two tropical regions. In general, the time scale for the development and decay of high rain events was faster in the mid-latitudes than the tropics. In particular, the mid-level stratiform convergence of the two mid-latitude regions developed much more quickly after peak rainfall than in the two tropical regions. It is not clear whether these differences arise from differences in the rates of convective development over land versus the ocean, from the larger value of the Coriolis parameter in mid-latitudes, or from the smaller size of the mid-latitude radiosonde arrays.

In mid-latitudes, rain events are associated with larger negative anomalies in surface pressure than those in the tropics, and lack the surface pressure increase that occurs after peak rainfall in the tropics. Within the Southeast United States region, rain events which occur in the evening are associated with larger reductions in surface pressure than those that occur during the day. It is not clear whether this pressure reduction is forced by the convection itself, or whether the lower surface pressure is associated with a more favorable synoptic environment for convective events at night. If the surface pressure reduction is indeed forced by convection, it may contribute to the observed diurnal cycle in surface pressure in this region.

Convective circulations impose perturbations in temperature, relative humidity, and surface pressure on the background atmosphere. The resulting anomalies in geopotential height generate, after some time lag, secondary large scale vertical motions which damp the temperature anomalies generated by the initial primary convective circulations. The overall effect of moist convection on the background atmosphere is therefore best understood in terms of an interplay between the primary circulations generated by the three main convective cloud types (congestus, deep, and stratiform) and their induced dry circulations. For example, we have shown that the development of large scale downward motion in the lower troposphere and upward motion in the upper troposphere after peak rainfall contribute to the erosion of the dominant local stratiform temperature response to convective events. Although this conceptual model of the interaction between the primary convective and secondary dry circulations was motivated by the anomaly patterns obtained from the Western Tropical Pacific region, the similarity of the anomaly patterns between the various regions suggests that it can be applied elsewhere.

The secondary dry circulations are likely to have a strong influence on the evolution of convective precipitation. In particular, the response of the dry deep circulation to the convective deep circulation is much faster than the response of the dry stratiform circulation to the convective stratiform circulation. As a result, the full depth warming and drying from deep convection are rapidly exported to larger spatial scales, and the stratiform temperature response dominates in the near field. The rapid export of the full depth heating and drying by the dry circulation helps prevent the reductions in CAPE that would otherwise occur during the intensification phase of deep convective events. It therefore functions as a positive feedback on the development of deep convection. Because of the longer time lag of the dry stratiform circulation, the onset of lower tropospheric subsidence in response to the convective stratiform circulation is delayed. This promotes the development of positive anomalies in column water and lower tropospheric relative humidity during high rain events.

We were able to calculate the vorticity and potential vorticity anomaly patterns in the Southeast China the Southeast United States regions. In both of these regions, high rain events are associated with negative anomalies in upper tropospheric relative and potential vorticity. These negative anomalies extend into the lower stratosphere. Below 400 hPa, convective events are associated with positive anomalies in both relative and potential vorticity. The vorticity change is consistent with the development of mid-level convergence during strong convective events. The mid-level positive PV anomaly is consistent with the local dominance of the stratiform heating mode. After peak rainfall, the mid-level positive PV anomaly is transported downward toward the surface by the dry stratiform circulation.

One objective in calculating anomaly patterns about high rain events is to provide observational targets for the development of improved convective parameterizations in climate models. For example, we have shown earlier that several climate models and reanalysis products have difficulty in simulating the observed temperature anomaly patterns about high rain events [*Mitovski et al*., 2010]. One of the difficulties in simulating the observed temperature response to convection is that the total temperature tendency is a small residual of the much larger temperature tendencies from the convective and dry circulations. Therefore, in addition to requiring that a convective parameterization generate the correct relative mix of congestus, deep, and stratiform circulations (or heating profiles) during the evolution of high rain events, it is also necessary that the dry induced circulations generated by the climate model exhibit the appropriate time lags. This requires, in part, that the climate model accurately simulates the observed geopotential height anomaly patterns which develop during high rain events, and that they have sufficient spatial and temporal resolution to resolve the induced dry dynamical circulations of the various heating modes. Difficulties in simulating the observed divergence response to high rain events, and in particular the mid-level divergence dipole, suggest that the dry dynamical response to convective heating is not realistically simulated in most climate models [*Mitovski et al*., 2010].

Acknowledgements

We thank the following institutions for making their data public: NASA GSFC (TRMM 3B42), NCDC (IGRA and ISH) and NCAR UCAR (COSMIC). This research was supported by a Research Grant from the Natural Sciences and Engineering Council of Canada

References

Anthes, R. A., and Coauthors (2008), The COSMIC/FORMOSAT-3 Mission: Early Results. *Bull. Amer. Meteor. Soc.*, **89**, 313–333, doi:10.1175/BAMS-89-3-313.

Benedict, J., and D. A. Randall (2007), Observed characteristics of the MJO relative to maximum rainfall. *J. Atmos. Sci*., **64**, 2332-2354, doi:10.1175/JAS3968.1.

Bister, M., and B. E. Mapes (2004), Effect of Vertical Dipole Temperature Anomalies on Convection in a Cloud Model. *J. Atmos. Sci*., **61**, 2092–2100, doi:10.1175/1520-0469(2004)061<2092:EOVDTA>2.0.CO;2.

Bister, M., and K. A. Emanuel (1997), The genesis of Hurricane Guillermo: TEXMEX analyses and a modeling study. *Mon. Wea. Rev*., **125**, 2662-2682, doi:10.1175/1520-0493(1997)125<2662:TGOHGT>2.0.CO;2.

Bretherton, C. S., P. K. Smolarkiewicz (1989), Gravity Waves, Compensating Subsidence and Detrainment around Cumulus Clouds. *J. Atmos. Sci*., **46**, 740–759, doi:10.1175/1520-0469(1989)046<0740:GWCSAD>2.0.CO;2.

Dai, A., F. Giorgi, and K. E. Trenberth (1999), Observed and model-simulated diurnal cycles of precipitation over the contiguous United States. *J. Geophys. Res.,* **104**, 6377-6402, doi:10.1029/98JD02720.

DeMott, C., D. A. Randall, and M. Khairoutdinov (2007), Convective precipitation variability as a tool for general circulation model analysis. *J. Climate,* **20**, 91-112, doi:10.1175/JCLI3991.1.

Durre, I., R. S. Vose, and D. B. Wuertz (2006), Overview of the integrated global radiosonde archive. *J. Climate,* **19**, 53-68, doi:10.1175/JCLI3594.1.

Emanuel, K.A. (1994), *Atmospheric Convection*, Oxford University Press, New York, 580 pp.

Folkins, I. (2009), A one-dimensional cloud model with trimodal convective outflow, *J. Climate*, **22**, 6437 - 6455, doi:10.1175/2009JCLI3134.1.

Gjorgjievska, S. and D. J. Raymond (2013), Interaction between dynamics and thermodynamics during tropical cyclogenesis. Submitted to *Atmos. Chem. Phys*.

Hertenstein, R. F. A., and W. H. Schubert (1991), Potential Vorticity Anomalies Associated with Squall Lines. *Mon. Wea. Rev*., **119**, 1663–1672, doi:10.1175/1520-0493(1991)119<1663:PVAAWS>2.0.CO;2.

Hohenegger, C., and B. Stevens (2013), Preconditioning Deep Convection with Cumulus Congestus. *J. Atmos. Sci*., **70**, 448–464, doi:10.1175/JAS-D-12-089.1.

Johnson, R.H., T. M. Rickenbach, S. A. Rutledge, P. E. Ciesielski, and W. H. Schubert (1999), Trimodal characteristics of tropical convection. *J. Climate*, **12**, 2397-2418, doi:10.1175/1520-0442(1999)012<2397:TCOTC>2.0.CO;2.

Kley, D., J. M. Russell III, and C. Phillips (Eds.) (2000), SPARC Assessment of upper tropospheric and stratospheric water vapor, WMO/TD-143, World Clim. Res. Programme, Geneva.

Kummerow, C., W. Barnes, T. Kozu, J. Shiue, and J. Simpson (1998), The Tropical Rainfall Measuring Mission (TRMM) Sensor Package. *J. Atmos. Oceanic Technol.,* **15**, 809-817, doi:10.1175/1520-0426(1998)015<0809:TTRMMT>2.0.CO;2.

Liu, Z., D. Ostrenga, W. Teng, and S. Kempler (2012), Tropical Rainfall Measuring Mission (TRMM) Precipitation Data and Services for Research and Applications. *Bull. Amer. Meteor. Soc.,* **93**, 1317-1325, doi:10.1175/BAMS-D-11-00152.1.

Lott, N., R. Baldwin, and P. Jones (2001), The FCC integrated surface hourly database: A new resource of global climate date. NOAA National Climatic Data Center Tech. Rep. 2001-01, 42 pp.

Mapes, B.E. (1997), Equilibrium vs. activation controls on large-scale variations of tropical deep convection. *The physics and parameterization of moist convection,* Kluwer Academic Publishers, Dordrecht, pp 321-358.

Mapes, B. E., and R.A. Houze, Jr. (1995), Diabatic divergence profiles in Western Pacific mesoscale convective systems. *J. Atmos. Sci.,* **52**, 1807-1828, doi:10.1175/1520-0469(1995)052<1807:DDPIWP>2.0.CO;2.

Mapes, B. E., S. Tulich, J. Lin, and P. Zuidema (2006), The mesoscale convection life cycle: Building block or prototype for large-scale tropical waves? *Dyn. Atmos. Oceans,* **42**, 3-29, doi:10.1016/j.dynatmoce.2006.03.003.

Mapes, B. E., et al. (2009), Virtual field campaigns on deep tropical convection in climate models. *J. Climate*, **22**, 244–257, doi:10.1175/2008JCLI2203.1.

Masunaga, H. (2012), A Satellite Study of the Atmospheric Forcing and Response to Moist Convection over Tropical and Subtropical Oceans. *J. Atmos. Sci*., **69**, 150–167, doi:10.1175/JAS-D-11-016.1.

Mitovski, T., I. Folkins, K. von Salzen, and M. Sigmond (2010), Temperature, relative humidity, and divergence response to high rainfall events in the tropics: Observations and models. *J. Climate,* **23**, 3613-3625, doi:10.1175/2010JCLI3436.1.

Nesbitt, S. W., and E. J. Zipser (2003), The Diurnal Cycle of Rainfall and Convective Intensity according to Three Years of TRMM Measurements. *J. Climate*, **16**, 1456–1475, doi:10.1175/1520-0442-16.10.1456.

Rapp, A. D., C. Kummerow, and L. D. Fowler (2011), Interactions between warm rain clouds and atmospheric preconditioning for deep convection in the tropics. *J. Geophys. Res*., **16**, D23210 doi:10.1029/2011JD016143.

Raymond, D. J., S. Sessions, A. Sobel, and Ž. Fuchs (2009), The mechanics of gross moist stability, *J. Adv. Model. Earth Syst*., 1, Article 9, 20 pp., doi:10.3894/JAMES.2009.1.9.

Schumacher, C., and R. A. Houze (2003), Stratiform Rain in the Tropics as Seen by the TRMM Precipitation Radar. *J. Climate*, **16**, 1739–1756, doi:10.1175/1520-0442(2003)016<1739:SRITTA>2.0.CO;2.

Sherwood, S. C., and R. Wahrlich (1999), Observed evolution of tropical deep convective events and their environment. *Mon. Wea. Rev.,* **127**, 1777-1795, doi:10.1175/1520-0493(1999)127<1777:OEOTDC>2.0.CO;2.

Sobel, A. H., J. Nilsson, and L. M. Polvani (2001), The Weak Temperature Gradient Approximation and Balanced Tropical Moisture Waves. *J. Atmos. Sci*., **58**, 3650–3665, doi:10.1175/1520-0469(2001)058<3650:TWTGAA>2.0.CO;2.

Sobel, A. H., S. E. Yuter, C. S. Bretherton, and G. N. Kiladis (2004), Large-scale meteorology and deep convection during TRMM KWAJEX. *Mon. Wea. Rev.,* **132**, 422–444, doi:10.1175/1520-0493(2004)132<0422:LMADCD>2.0.CO;2.

Takayabu, Y. N., K.-M. Lau, and C.-H. Sui (1996), Observation of a quasi 2-day wave during TOGA COARE. *Mon. Wea. Rev.,* **124**, 1892-1913, doi:10.1175/1520-0493(1996)124<1892:OOAQDW>2.0.CO;2.

Thompson, R. M., Jr., S. W. Payne, E. E. Recker, and R. J. Reed (1979), Structure and properties of synoptic-scale wave disturbances in the intertropical convergence zone of the eastern Atlantic. *J. Atmos. Sci.,* **36**, 53-72, doi:10.1175/1520-0469(1979)036<0053:SAPOSS>2.0.CO;2.

Xie, F., Wu, D. L., Ao, C. O., Mannucci, A. J., and Kursinski, E. R. (2012), Advances and limitations of atmospheric boundary layer observations with GPS occultation over southeast Pacific Ocean. *Atmos. Chem. Phys*., **12**, 903-918, doi:10.5194/acp-12-903-2012.

Zipser, E. J. (1977), Mesoscale and convective-scale downdrafts as distinct components of a squall-line structure. *Mon. Wea. Rev*., **105**, 1568 – 1589, doi:10.1175/1520-0493(1977)105<1568:MACDAD>2.0.CO;2.

Zuidema, P. (1998), The 600 – 800 mb minimum in tropical cloudiness observed during TOGA COARE. *J. Atmos. Sci*., **55**, 2220 – 2228, doi:10.1175/1520-0469(1998)055<2220:TMMITC>2.0.CO;2.

Zuluaga, M. D., and R. A. Houze, Jr. (2013) Evolution of the population of precipitating convective systems over the Equatorial Indian Ocean in Active Phases of the Madden-Julian Oscillation. *J. Atmos Sci*., in press, doi:10.1175/JAS-D-12-0311.1.

Figure Captions

Figure 1. Open squares refer to the co-located IGRA radiosonde station and ISH surface weather stations used to construct the anomaly patterns. The triangles show the radiosonde arrays used to calculate the mass divergence, relative vorticity, and potential vorticity anomaly patterns. The large rectangles show the regions within which rain events were chosen to calculate the radial variation of temperature and relative humidity about high rain events.

Figure 2. (upper) The variation in mean rainfall during the growth and decay of the TRMM 3B42 2x2 high rain events within each region. (lower) The radial variation in mean rainfall about the high rain events.

Figure 3. (upper) The variation in TRMM 3B42 2x2-degree rainfall with local solar time, averaged over the radiosonde locations of each region shown in Figure 1. (lower) The diurnal variation in the number of high rain events within each 3 hour time bin, calculated from all rain events used in the construction of the temperature anomaly patterns.

Figure 4. The number of available soundings, at each local solar time, within 48 hours of the rainfall events used in the construction of the temperature anomaly patterns. Different colors refer to different regions.

Figure 5. (a), (b), (c), and (d) show temperature anomaly patterns about the TRMM high rain events, calculated using IGRA radiosonde profiles from each region. (d) and (f) show temperature anomaly patterns calculated using the COSMIC GPS temperature profiles.

Figure 6. Within each figure, the dotted line refers to an anomaly profile calculated using 1-h ISH surface data, while the solid lines refer to anomaly profiles calculated using 12-h IGRA radiosonde data. (upper row) The variation of the surface temperature anomaly during high rain events. (middle row) The variation of surface relative humidity anomaly during high rain events. (bottom row) The variation in the surface pressure anomaly during high rain events. Each column refers to a different region with from left to right: the Tropical Western Pacific, Tropical Brazil, Southeast USA, and Southeast China regions.

Figure 7. (a) The black curve of the top panel shows the diurnal variation in the surface pressure anomaly, plotted against local solar time, of the surface stations within the Southeast United States region shown in Figure 1 (June, July, and August). The red curve was obtained from the subset of surface pressure measurements at which the local rain rate of each surface station exceeded 1.0 mm/h; (b) The solid black curve shows the surface pressure anomaly about high rain events constructed using radiosonde measurements launched at 6 LT only. The red curve shows the surface pressure anomaly about high rain constructed from radiosonde measurements at 18 LT only. The black dashed line shows the combined surface pressure anomaly of the two radiosonde launch times. (c) Each curve shows the surface pressure response, calculated using ISH surface station data within the Southeast United States region, to TRMM rain events occurring at a particular time. For each curve, the local time of the TRMM rain events is shown in the legend. The circles in the middle panel indicate the local time of the rain events about which the pressure anomaly was calculated. For example, the red circles of the middle panel indicate surface pressure anomalies calculated from radiosondes launched at 18 LT, from rain events at 15 LT. Each red circle of the middle panel corresponds to a red circle in the lower panel, which indicates the effect of rain occurring events at that time on the surface pressure anomaly. In general, maxima in the curves of the middle panel occur at times when the corresponding rain events have a reduced impact on surface pressure, and vice versa.

Figure 8. The radial distribution of the temperature anomaly about high rain events in each region. The horizontal axis refers to the radial distance between a radiosonde location and a TRMM high rain event. The patterns were constructed from radiosonde launches within 3 h of a TRMM rain event.

Figure 9. Each figure shows the effect of local high rain events on the relative humidity of the background atmosphere in each region. The horizontal axis refers to time since peak rainfall.

Figure 10. The radial distribution of the relative humidity anomaly about high rain events in each region. The horizontal axis refers to the radial distance between a radiosonde location and a TRMM high rain event. The patterns were constructed from radiosonde launches within 3 h of a TRMM rain event.

Figure 11. (upper) The variation in total column water vapor about high rain events in each region. (lower) The variation in the total column water vapor anomaly. The total column water vapor is a vertical sum of the water vapor between 1000 and 200 hPa, as measured by a radiosonde profile.

Figure 12. (upper) The response of boundary layer CAPE to high rain events in the Western Tropical Pacific and Southeast United States regions. The horizontal axis refers to time since peak rainfall. (lower) Similar to the upper panels, except showing the CAPE anomaly.

Figure 13. The effect of high rain events on the anomaly in geopotential height (GPHT) of each region. The horizontal axis refers to time since peak rainfall.

Figure 14. The effect of high rain events on the mass divergence anomaly of each region. The horizontal axis refers to time since peak rainfall.

Figure 15. The effect of high rain events on the atmospheric stability of each region. The horizontal axis refers to time since peak rainfall.

Figure 16. The effect of high rain events on the relative vorticity anomaly, calculated from radiosonde arrays in the Southeast United States and China. The horizontal axis refers to time since peak rainfall.

Figure 17. (a) and (b) show the vertical evolution of Potential Vorticity (PV) about high rain events, as calculated from radiosonde arrays in the Southeast United States and China regions. The horizontal axis refers to time since peak rainfall. (c) and (d) show the potential vorticity anomaly about high rain events. The potential vorticity is expressed in potential vorticity units (PVU), where $1\ \mathrm{PVU} = 10^{-6} \mathrm{m}^2\mathrm{s}^{-1}\mathrm{K}\mathrm{kg}^{-1}$.

Figure 18. (a) The observed temperature tendency pattern (dT/dt), calculated from the Western Tropical Pacific temperature anomaly patterns shown in Figure 5(a). (b) The temperature tendency pattern due to vertical advection, calculated from the vertical pressure velocity and stability anomaly patterns. (c) The relative humidity tendency pattern (dRH/dt) calculated from the Western Tropical Pacific relative humidity pattern shown in Figure 9(a). (d) The vertical pressure velocity calculated from the Western Pacific divergence anomaly pattern shown in Figure 14(a).

Figure 19. (upper) The mass weighted column heating rate about rain events in the Western Tropical Pacific region, calculated from the temperature anomaly patterns shown in Figure 5(a). The horizontal axis refers to time since peak rainfall. (lower) The mass divergence about high rain

events along particular pressure surfaces, derived from the mass divergence anomaly patterns shown in Figure 14(a).

Figure 20. (a) The primary convective circulations associated with congestus, deep, and stratiform clouds. Red arrows refer to heating (descent in the background atmosphere) while blue arrows refer to cooling (ascent in the background atmosphere). (b) The induced dry circulations associated with the convective circulations of each cloud type shown in (a). Inflows and outflows at the boundary of the convecting region (radiosonde array) are indicated by horizontal arrows. (c) The direct convective circulation associated with a precipitating cloud with no downdrafts. (d) The induced dry circulation generated by the convective circulation shown in (c).

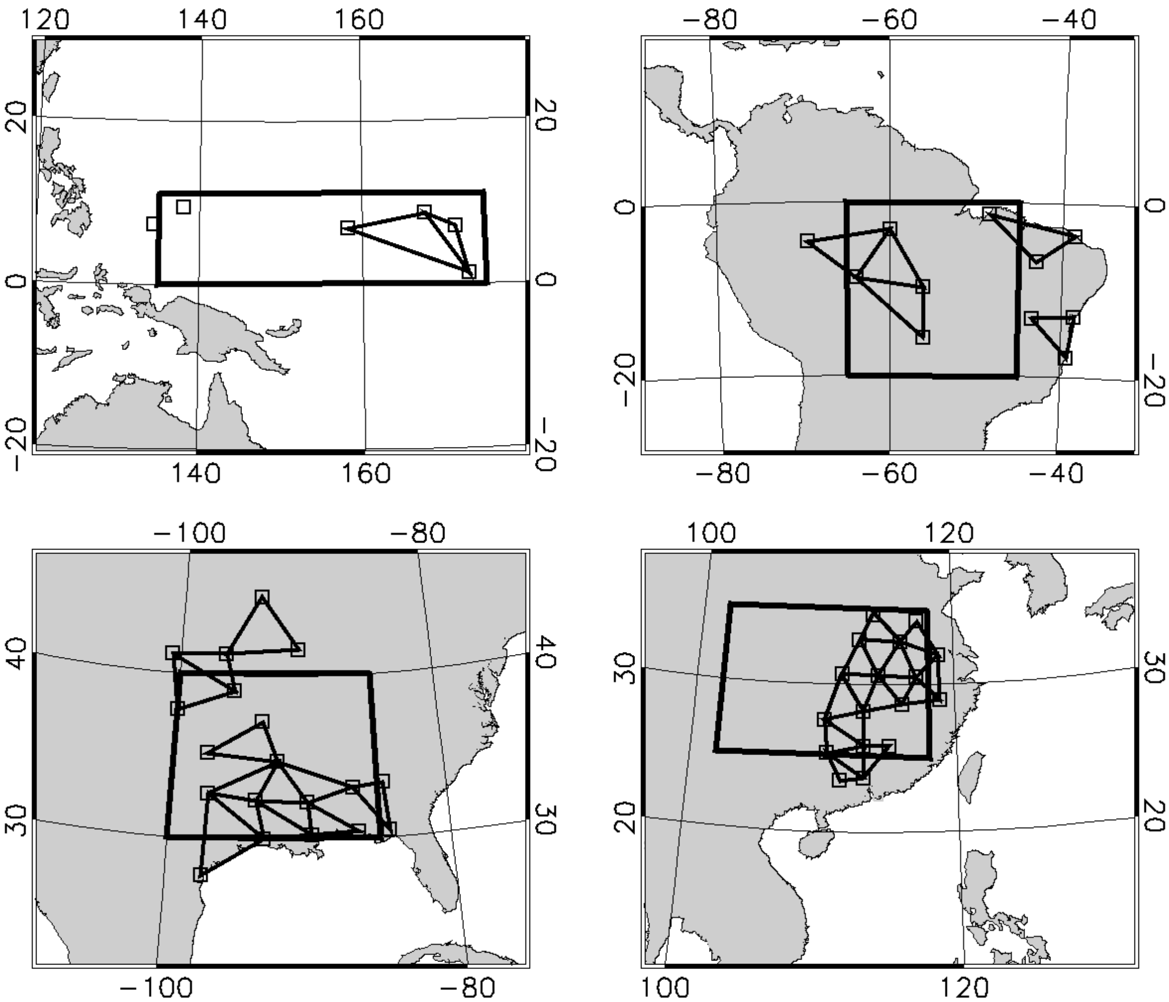

Figure 1. Open squares refer to the co-located IGRA radiosonde station and ISH surface weather stations used to construct the anomaly patterns. The triangles show the radiosonde arrays used to calculate the mass divergence, relative vorticity, and potential vorticity anomaly patterns. The large rectangles show the regions within which rain events were chosen to calculate the radial variation of temperature and relative humidity about high rain events.

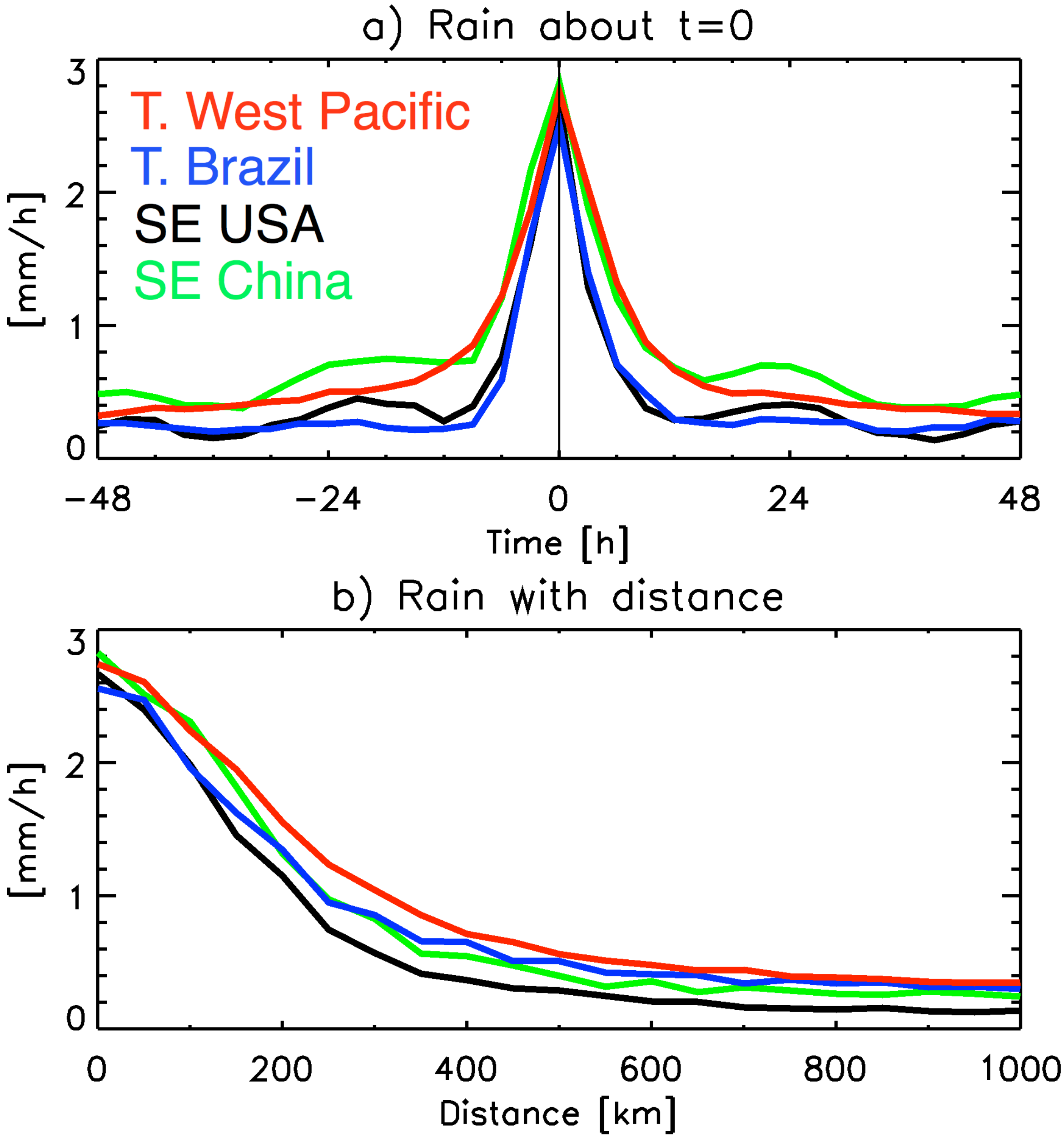

Figure 2. (upper) The variation in mean rainfall during the growth and decay of the TRMM 3B42 2x2 high rain events within each region. (lower) The radial variation in mean rainfall about the high rain events.

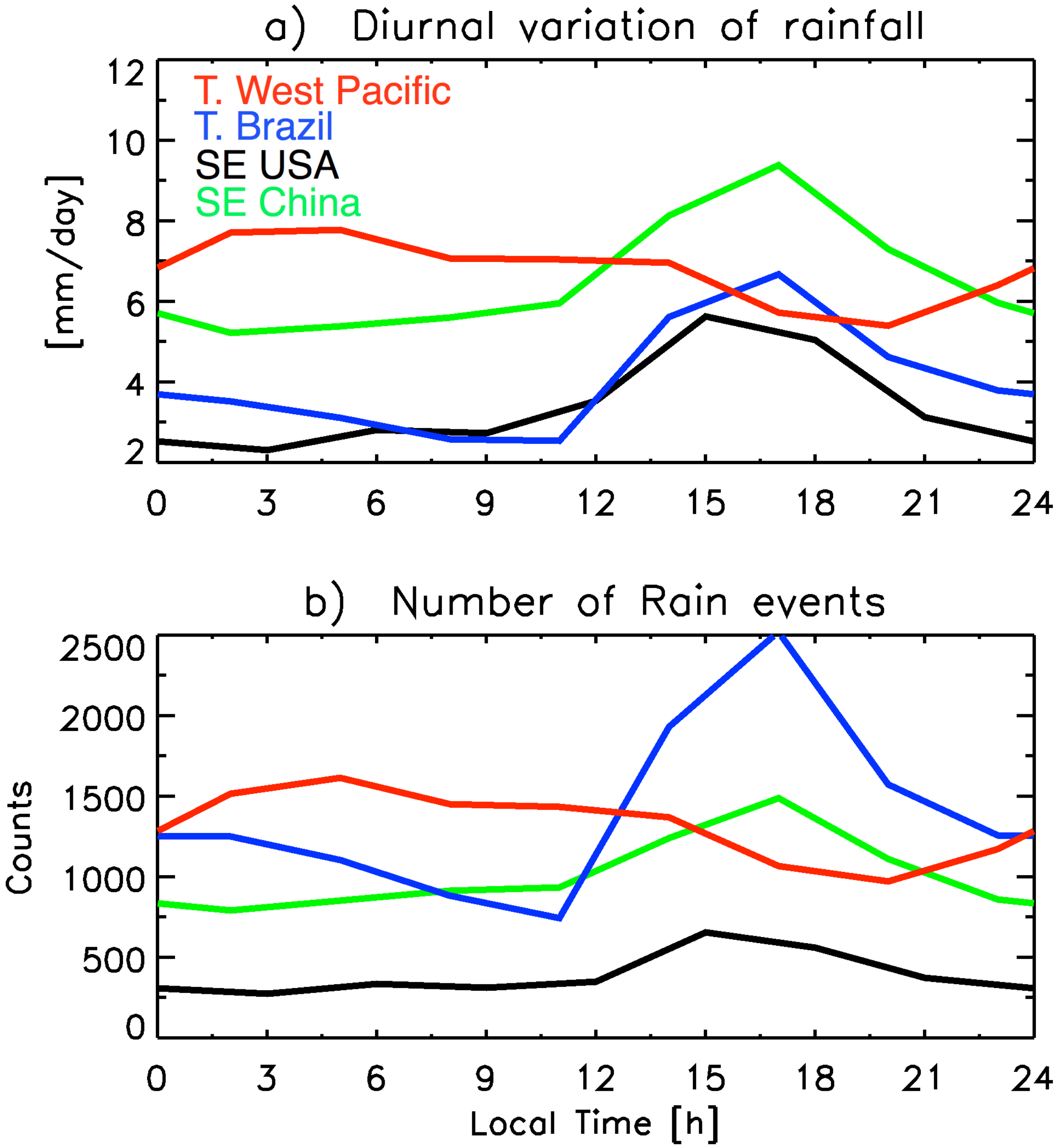

977

978 Figure 3. (upper) The variation in TRMM 3B42 2x2-degree rainfall with local solar time, averaged

979 over the radiosonde locations of each region shown in Figure 1. (lower) The diurnal variation in the

980 number of high rain events within each 3 hour time bin, calculated from all rain events used in the

981 construction of the temperature anomaly patterns.

982

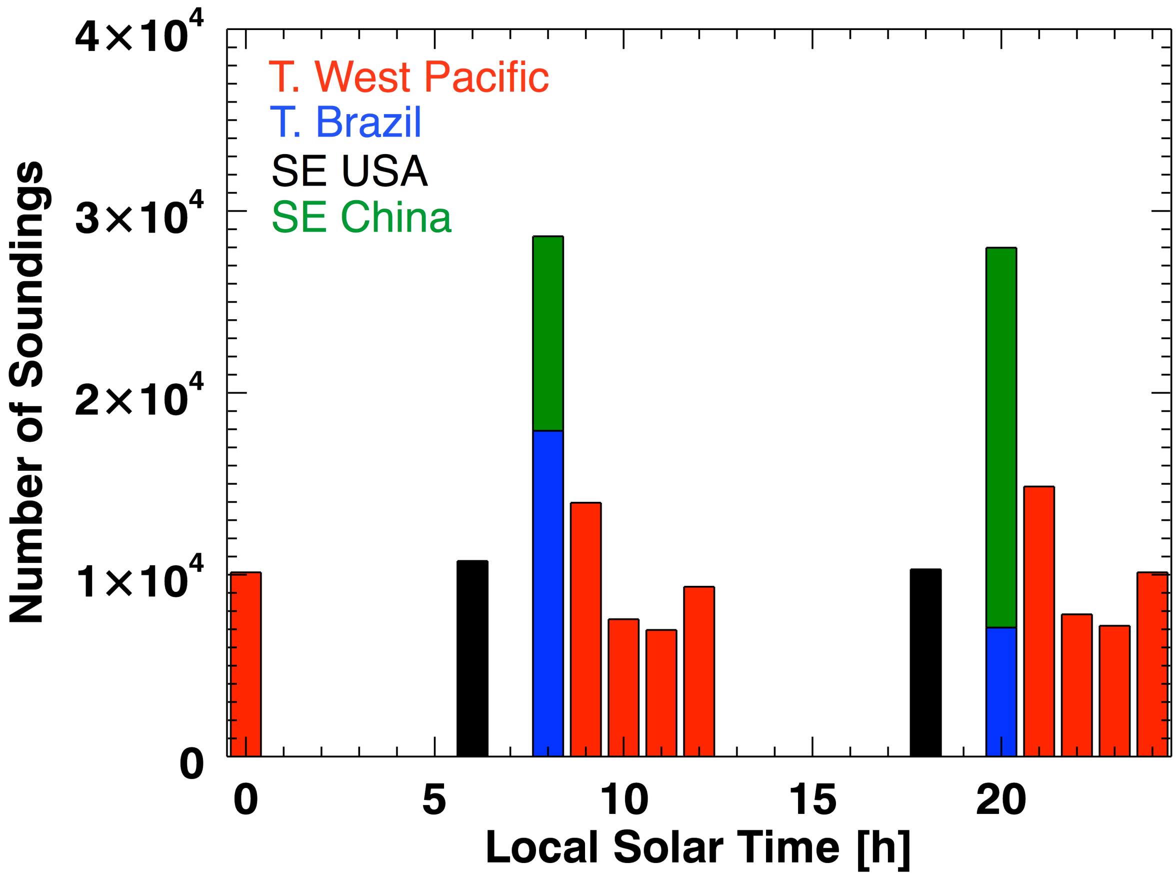

Figure 4. The number of available soundings, at each local solar time, within 48 hours of the rainfall events used in the construction of the temperature anomaly patterns. Different colors refer to different regions.

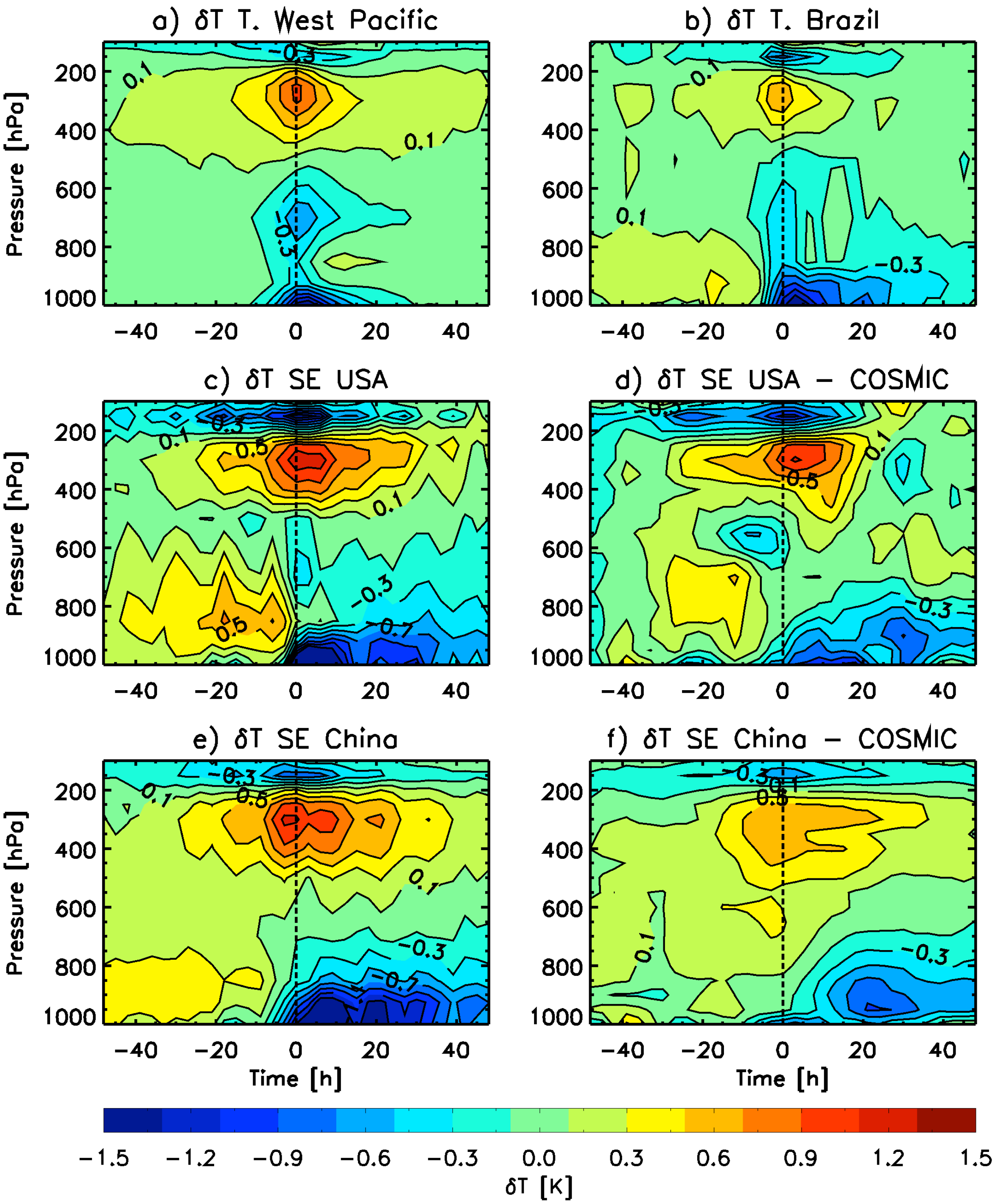

Figure 5. (a), (b), (c), and (e) show temperature anomaly patterns about the TRMM high rain events, calculated using IGRA radiosonde profiles from each region. (d) and (f) show temperature anomaly patterns calculated using the COSMIC GPS temperature profiles.

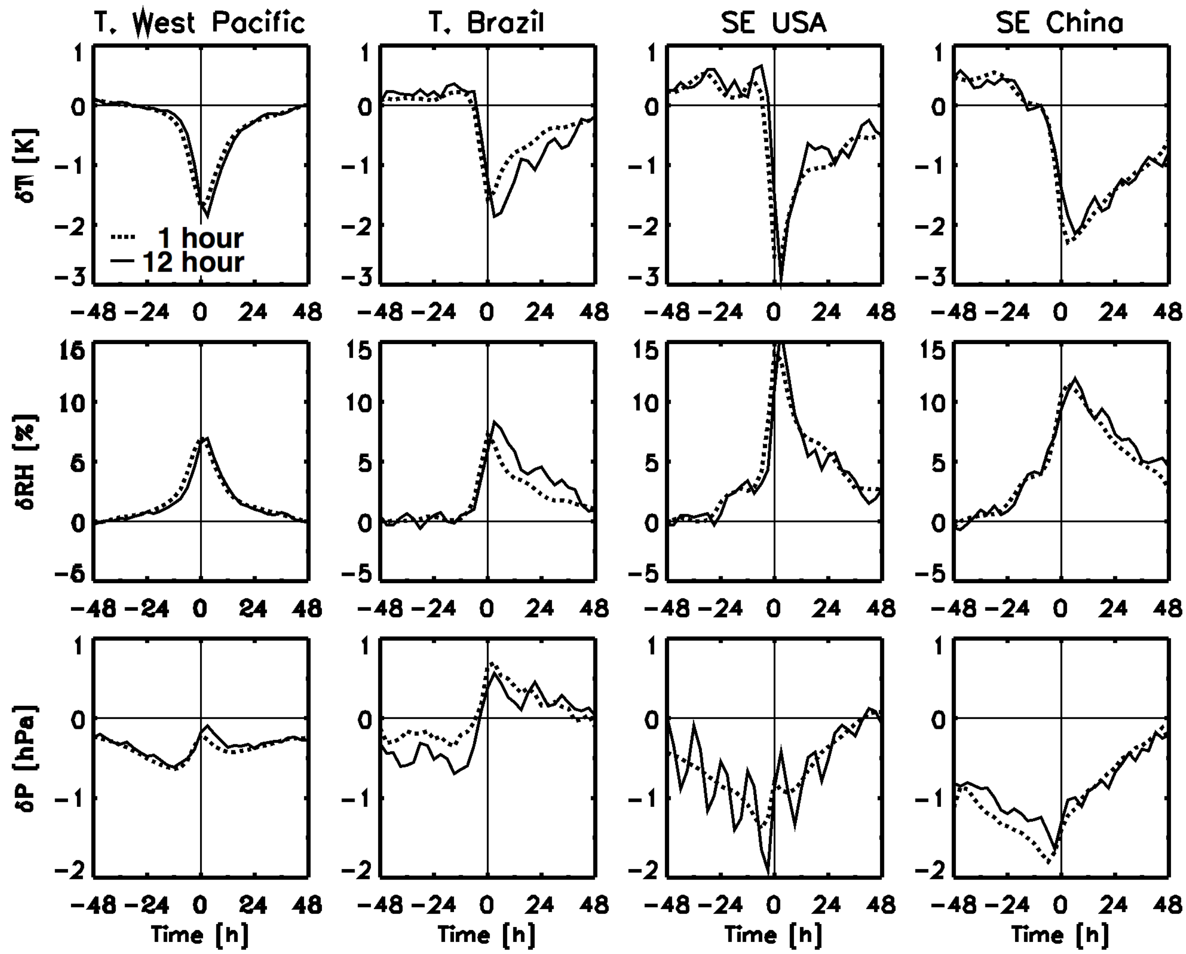

Figure 6. Within each figure, the dotted line refers to an anomaly profile calculated using 1-h ISH surface data, while the solid lines refer to anomaly profiles calculated using 12-h IGRA radiosonde data. (upper row) The variation of the surface temperature anomaly during high rain events. (middle row) The variation of surface relative humidity anomaly during high rain events. (bottom row) The variation in the surface pressure anomaly during high rain events. Each column refers to a different region with from left to right: the Tropical Western Pacific, Tropical Brazil, Southeast USA, and Southeast China regions.

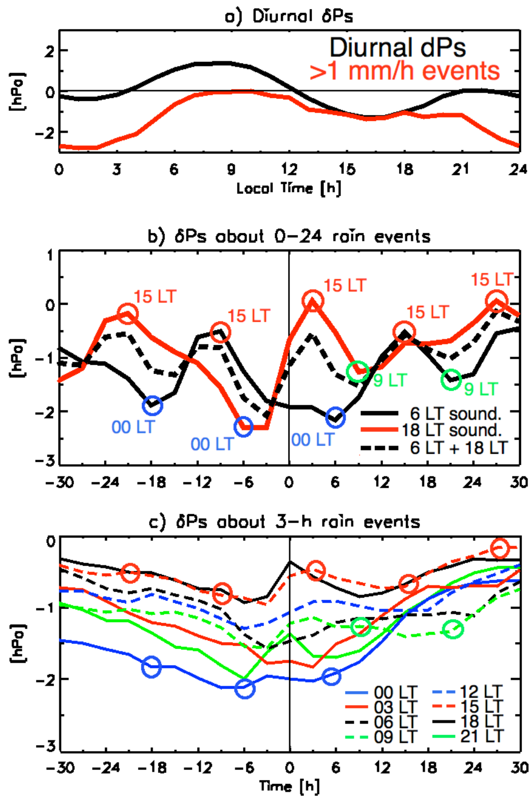

Figure 7. (a) The black curve of the top panel shows the diurnal variation in the surface pressure anomaly, plotted against local solar time, of the surface stations within the Southeast United States region shown in Figure 1 (June, July, and August). The red curve was obtained from the subset of surface pressure measurements at which the local rain rate of each surface station exceeded 1.0 mm/h; (b) The solid black curve shows the surface pressure anomaly about high rain events constructed using radiosonde measurements launched at 6 LT only. The red curve shows the surface pressure anomaly about high rain constructed from radiosonde measurements at 18 LT only. The black dashed line shows the combined surface pressure anomaly of the two radiosonde launch times. (c) Each curve shows the surface pressure response, calculated using ISH surface station data within the Southeast United States region, to TRMM rain events occurring at a particular time. For each curve, the local time of the TRMM rain events is shown in the legend. The circles in the middle panel indicate the local time of the rain events about which the pressure anomaly was calculated. For example, the red circles of the middle panel indicate surface pressure anomalies calculated from radiosondes launched at 18 LT, from rain events at 15 LT. Each red circle of the middle panel corresponds to a red circle in the lower panel, which indicates the effect of rain occurring events at that time on the surface pressure anomaly. In general, maxima in the curves of the middle panel occur at times when the corresponding rain events have a reduced impact on surface pressure, and vice versa.

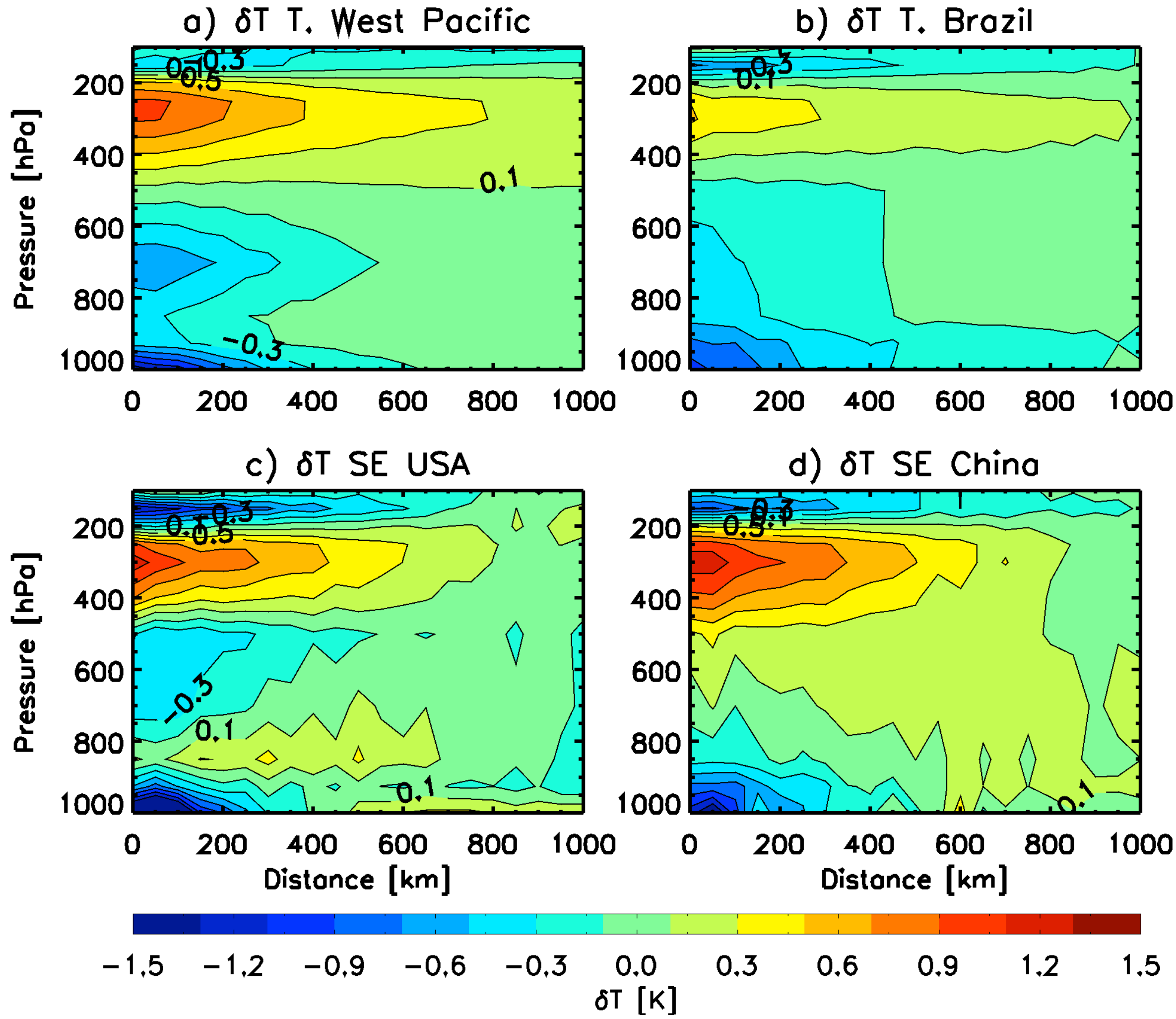

Figure 8. The radial distribution of the temperature anomaly about high rain events in each region. The horizontal axis refers to the radial distance between a radiosonde location and a TRMM high rain event. The patterns were constructed from radiosonde launches within 3 h of a TRMM rain event.

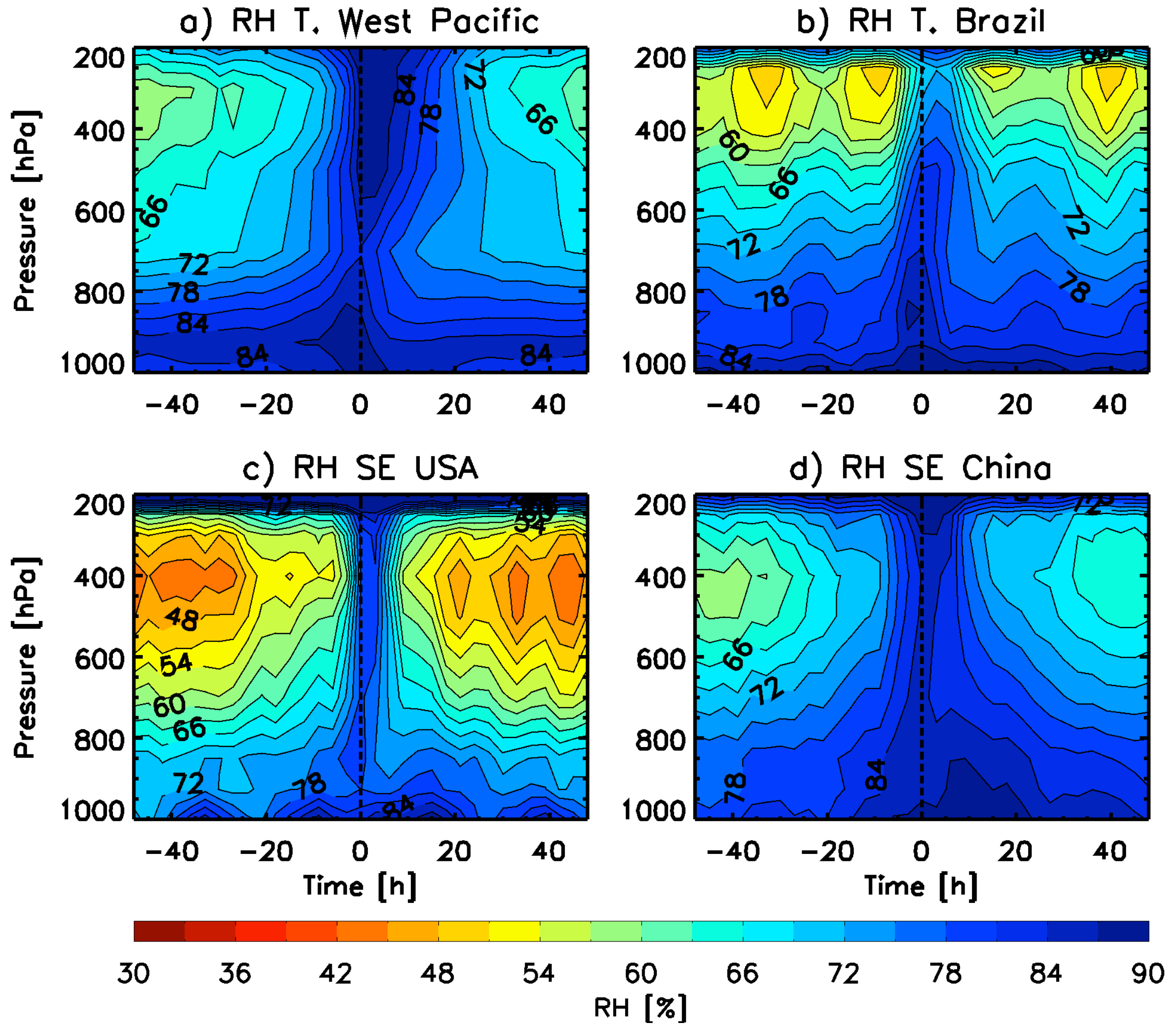

Figure 9. Each figure shows the effect of local high rain events on the relative humidity of the background atmosphere in each region. The horizontal axis refers to time since peak rainfall.

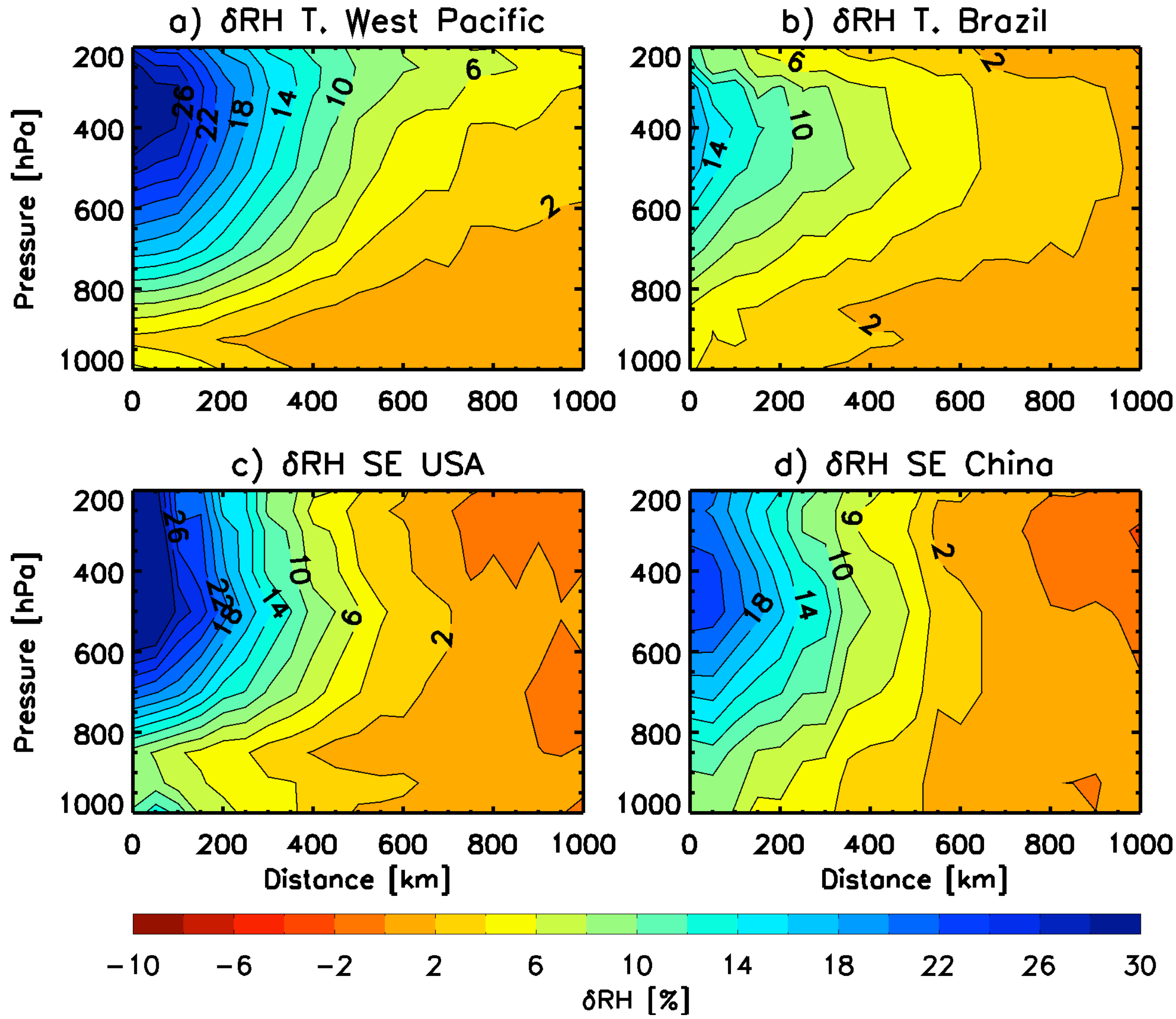

Figure 10. The radial distribution of the relative humidity anomaly about high rain events in each region. The horizontal axis refers to the radial distance between a radiosonde location and a TRMM high rain event. The patterns were constructed from radiosonde launches within 3 h of a TRMM rain event.

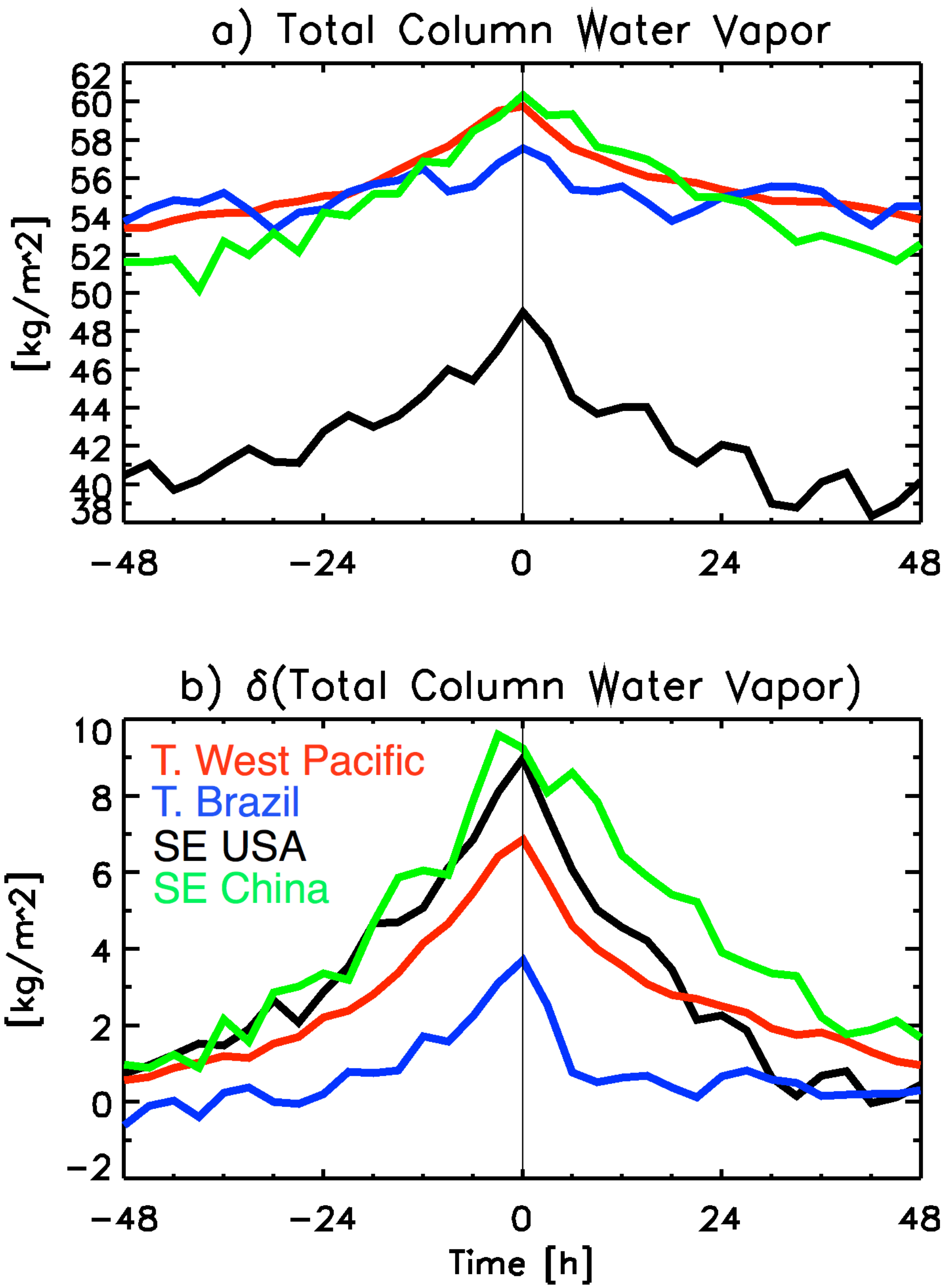

Figure 11. (upper) The variation in total column water vapor about high rain events in each region. (lower) The variation in the total column water vapor anomaly. The total column water vapor is a vertical sum of the water vapor between 1000 and 200 hPa, as measured by a radiosonde profile.

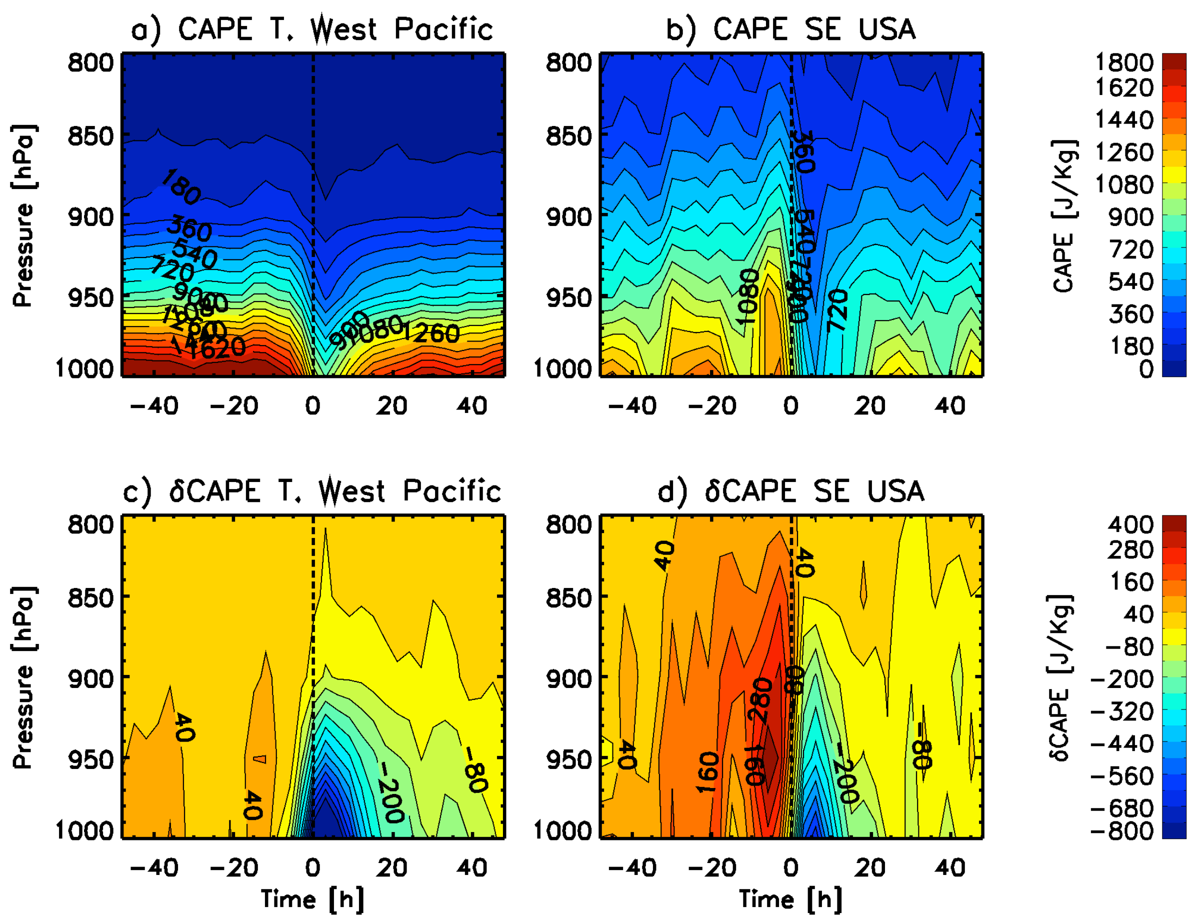

Figure 12. (upper) The response of boundary layer CAPE to high rain events in the Western Tropical Pacific and Southeast United States regions. The horizontal axis refers to time since peak rainfall. (lower) Similar to the upper panels, except showing the CAPE anomaly.

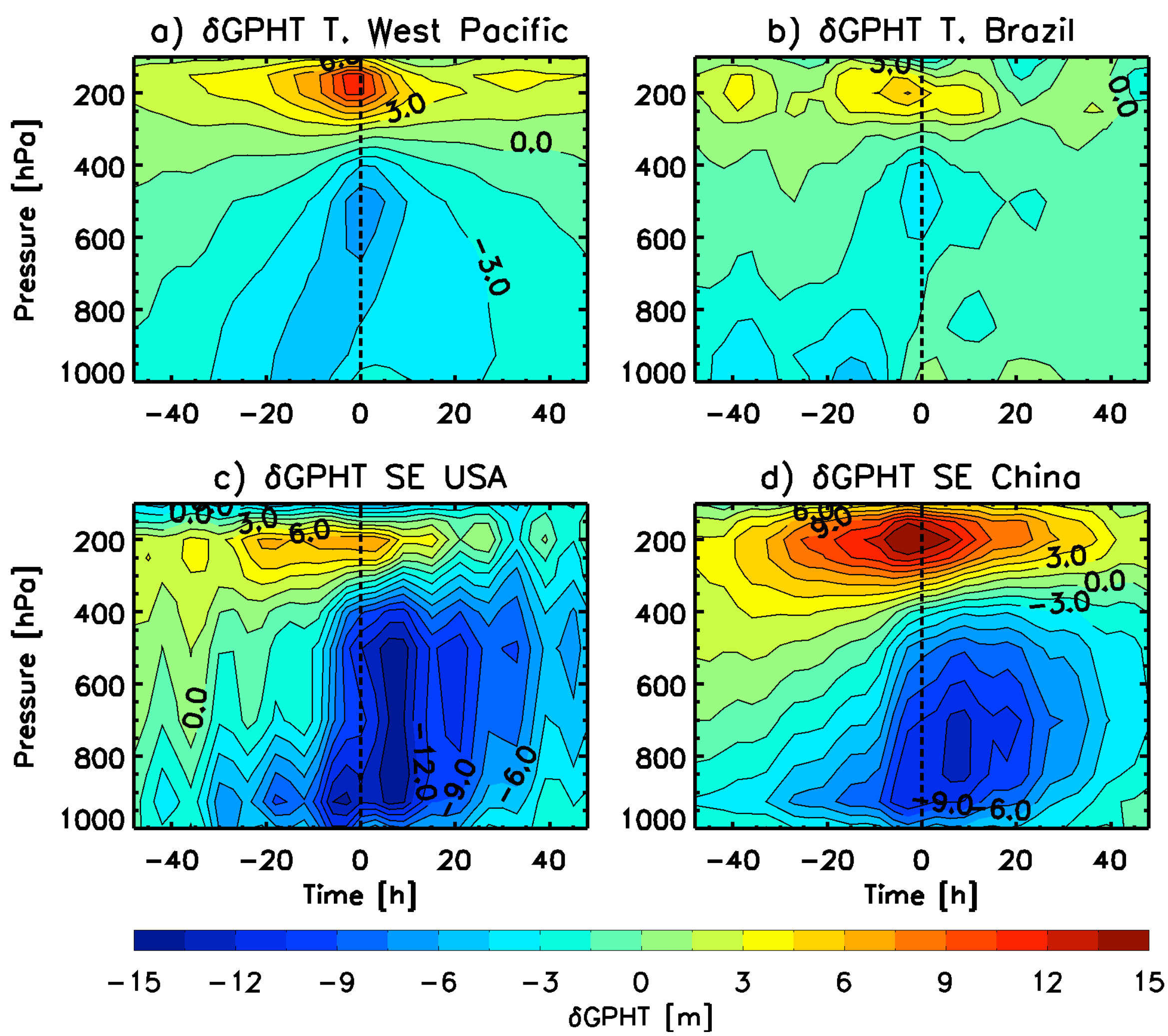

Figure 13. The effect of high rain events on the anomaly in geopotential height (GPHT) of each region. The horizontal axis refers to time since peak rainfall.

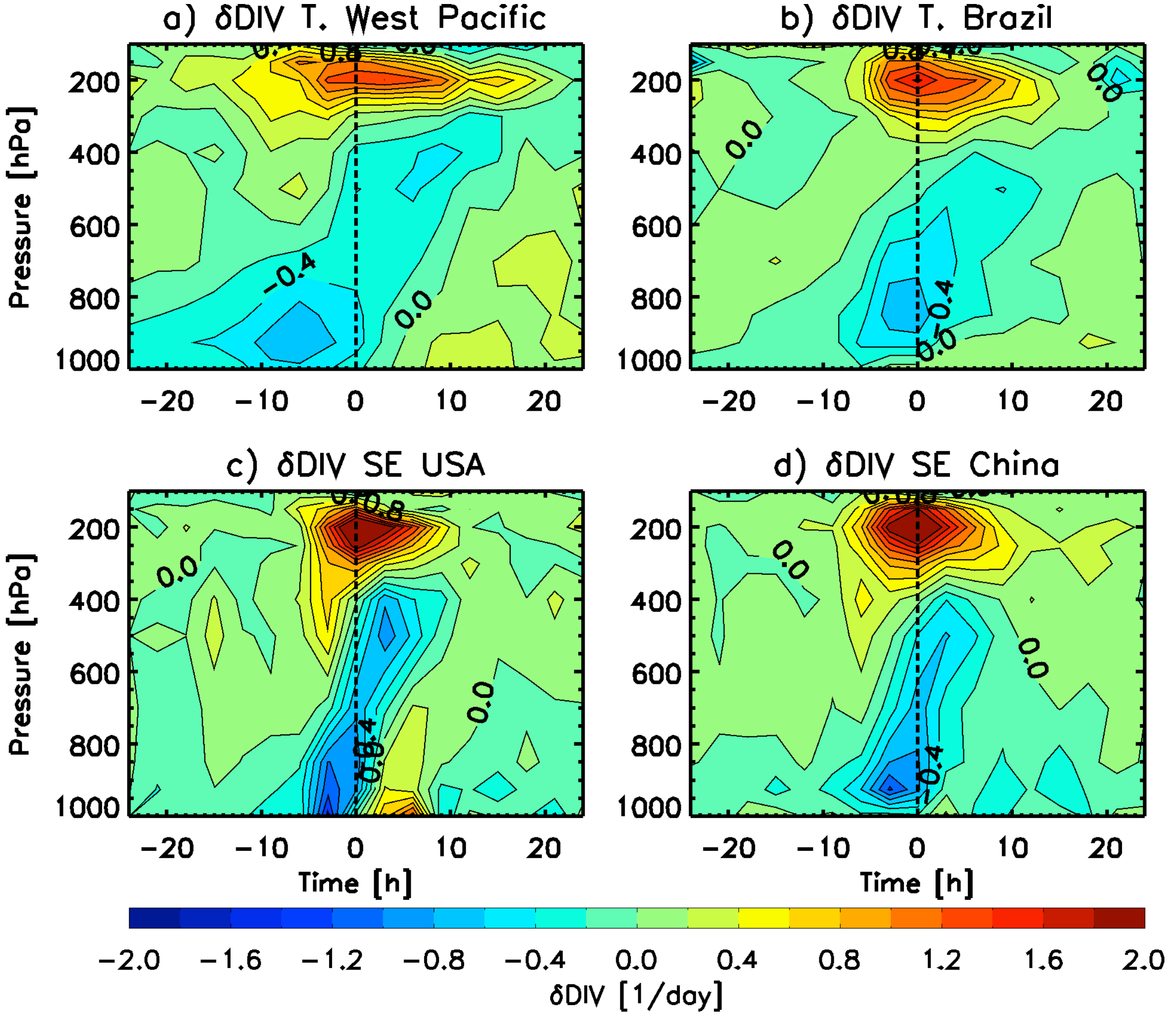

Figure 14. The effect of high rain events on the mass divergence anomaly of each region. The horizontal axis refers to time since peak rainfall.

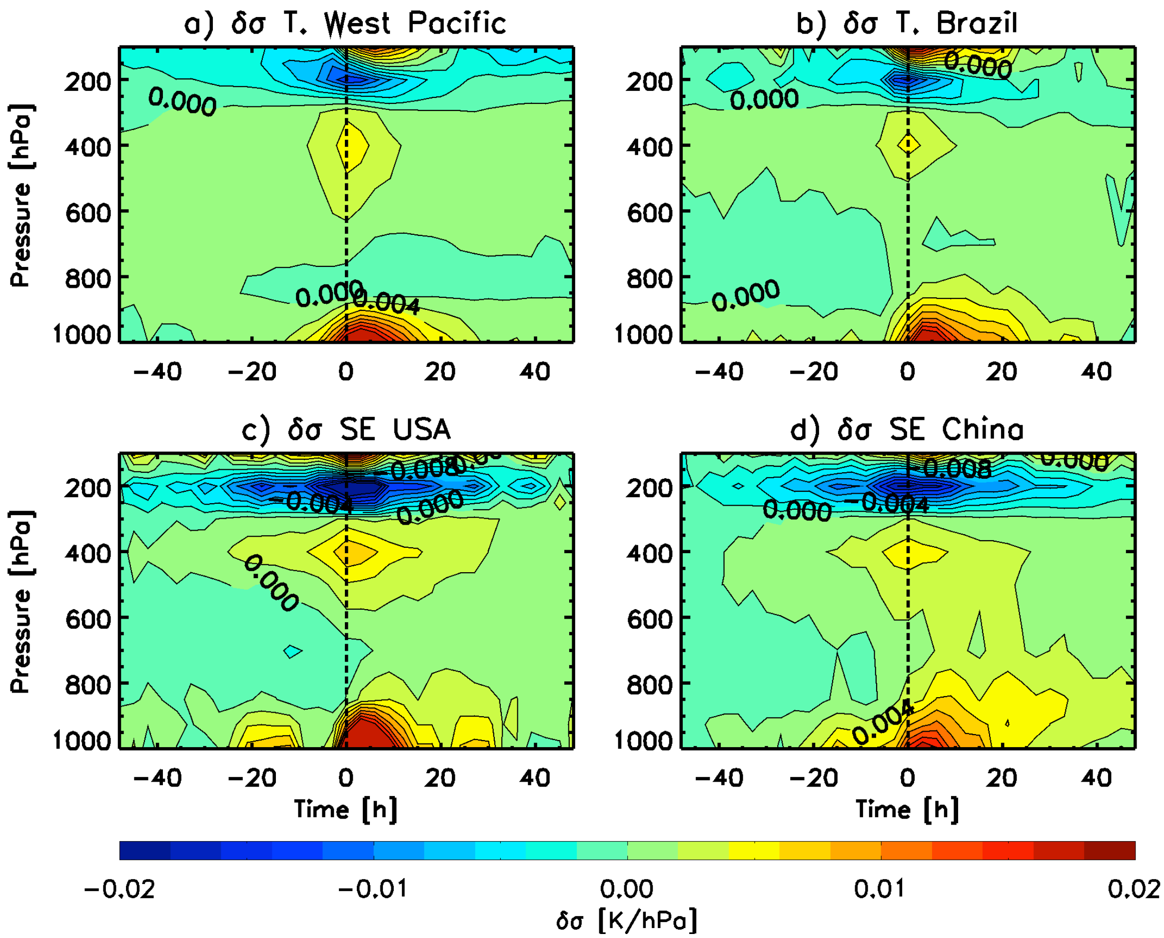

Figure 15. The effect of high rain events on the atmospheric stability of each region. The horizontal axis refers to time since peak rainfall.

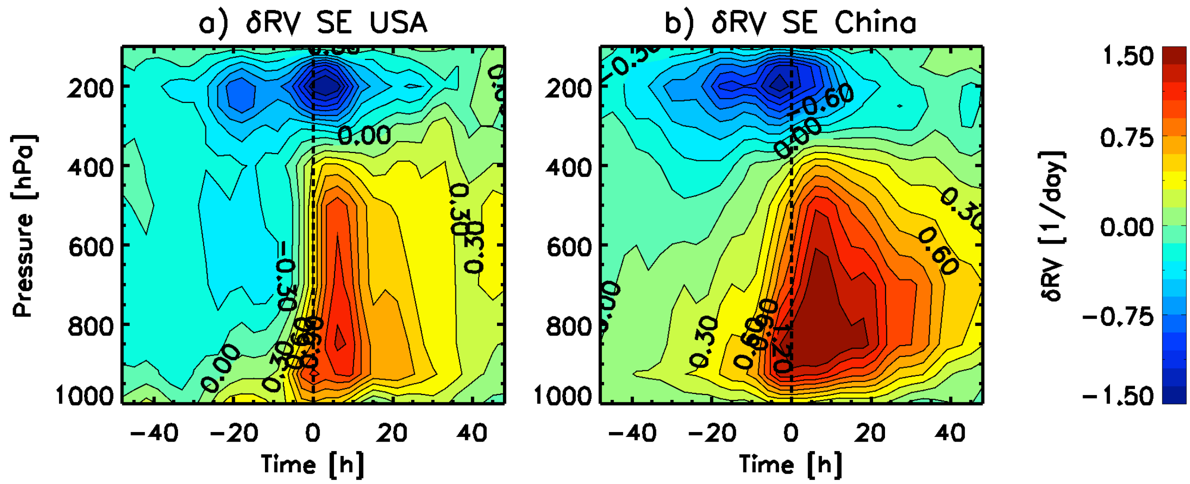

Figure 16. The effect of high rain events on the relative vorticity anomaly, calculated from radiosonde arrays in the Southeast United States and China. The horizontal axis refers to time since peak rainfall.

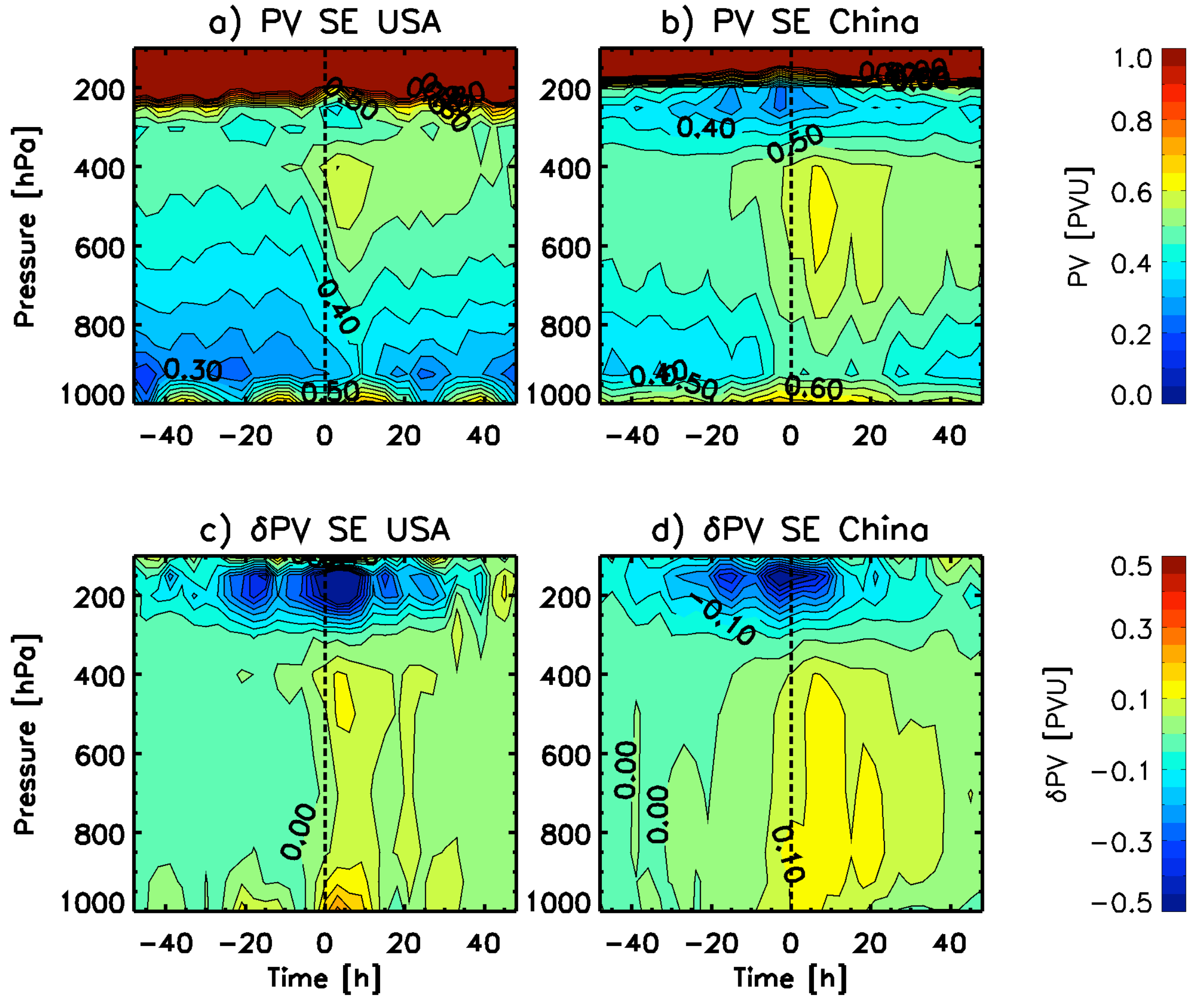

Figure 17. (a) and (b) show the vertical evolution of Potential Vorticity (PV) about high rain events, as calculated from radiosonde arrays in the Southeast United States and China regions. The horizontal axis refers to time since peak rainfall. (c) and (d) show the potential vorticity anomaly about high rain events. The potential vorticity is expressed in potential vorticity units (PVU), where 1 PVU $=10^{-6} m^2 s^{-1} K kg^{-1}$.

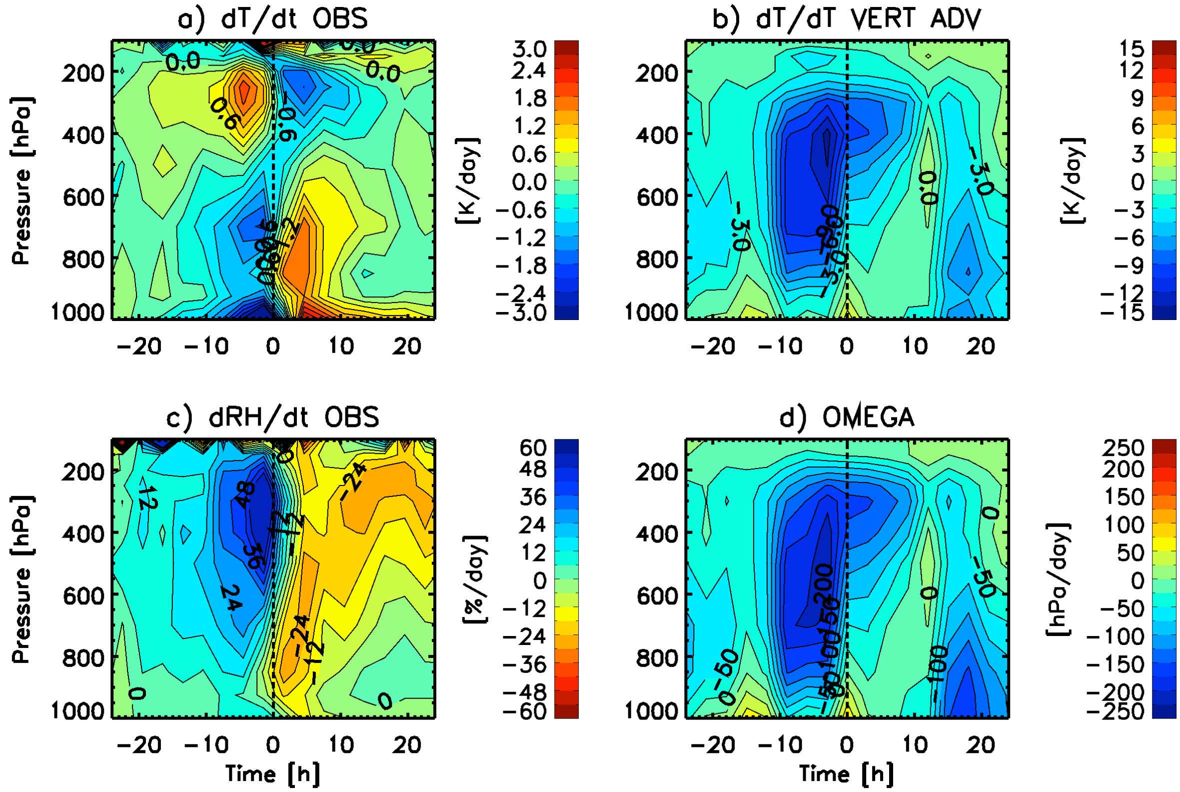

Figure 18. (a) The observed temperature tendency pattern (dT/dt), calculated from the Western Tropical Pacific temperature anomaly patterns shown in Figure 5(a). (b) The temperature tendency pattern due to vertical advection, calculated from the vertical pressure velocity and stability anomaly patterns. (c) The relative humidity tendency pattern (dRH/dt) calculated from the Western Tropical Pacific relative humidity pattern shown in Figure 9(a). (d) The vertical pressure velocity calculated from the Western Pacific divergence anomaly pattern shown in Figure 14(a).

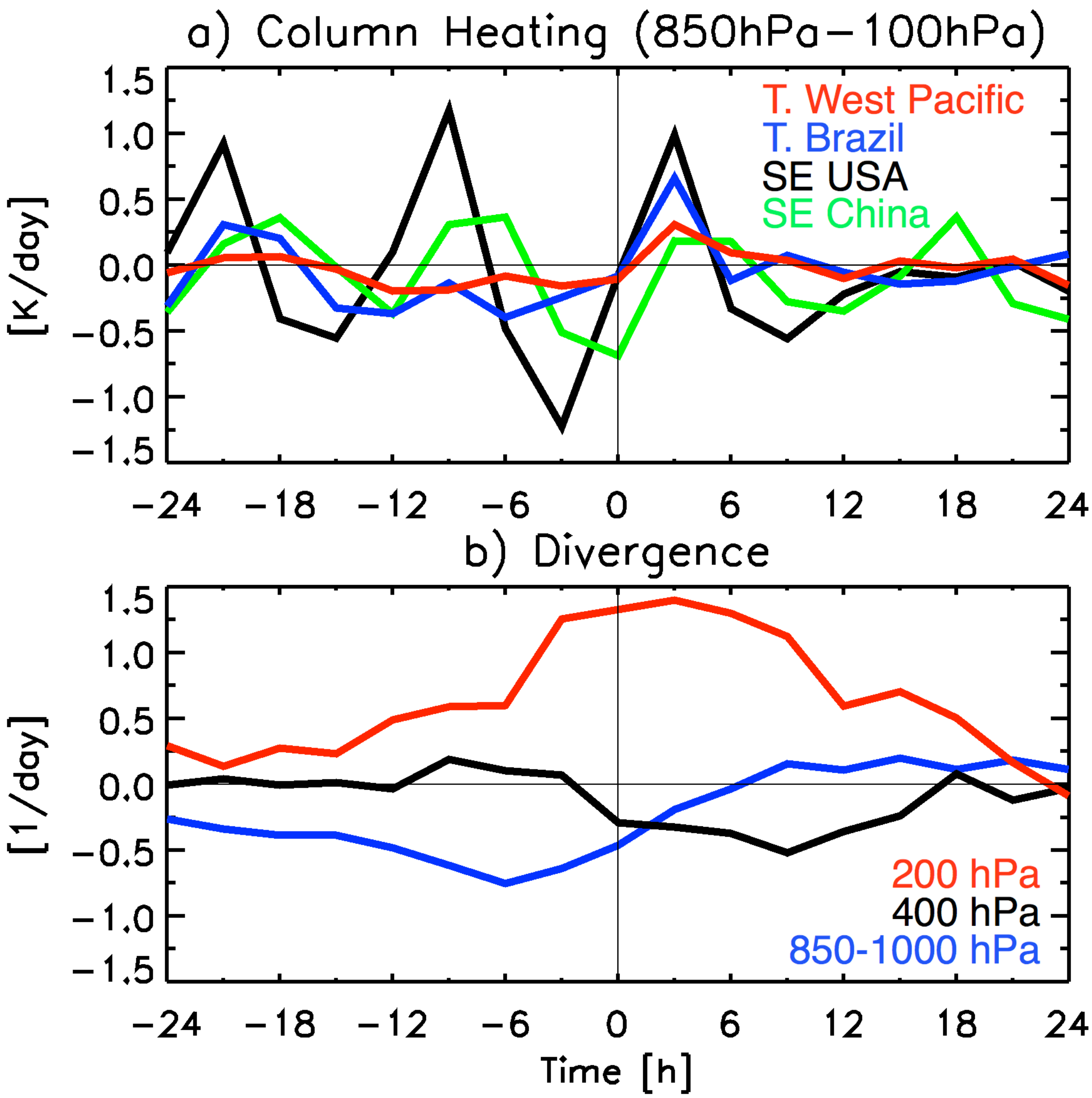

1081

1082 Figure 19. (upper) The mass weighted column heating rate about rain events in the Western
1083 Tropical Pacific region, calculated from the temperature anomaly patterns shown in Figure 5(a).
1084 The horizontal axis refers to time since peak rainfall. (lower) The mass divergence about high rain
1085 events along particular pressure surfaces, derived from the mass divergence anomaly patterns
1086 shown in Figure 14(a).

1087

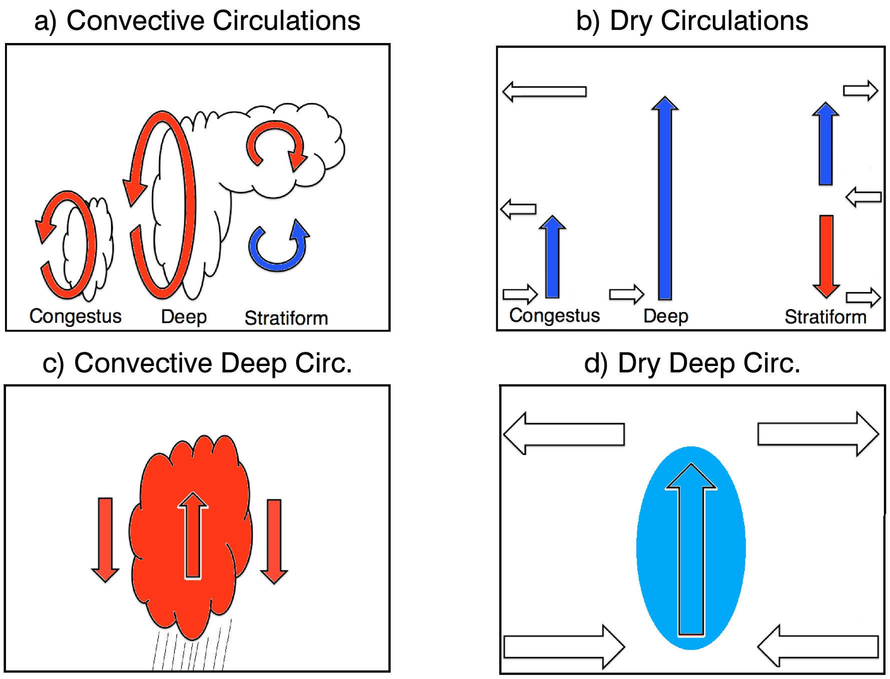

Figure 20. (a) The primary convective circulations associated with congestus, deep, and stratiform clouds. Red arrows refer to heating (descent in the background atmosphere) while blue arrows refer to cooling (ascent in the background atmosphere). (b) The induced dry circulations associated with the convective circulations of each cloud type shown in (a). Inflows and outflows at the boundary of the convecting region (radiosonde array) are indicated by horizontal arrows. (c) The direct convective circulation associated with a precipitating cloud with no downdrafts. (d) The induced dry circulation generated by the convective circulation shown in (c).